

UNIVERSITY OF CALIFORNIA  
SANTA CRUZ

**STRATIFIED ROTATIONAL INSTABILITIES AT LOW PÉCLET  
NUMBER**

A dissertation submitted in partial satisfaction of the  
requirements for the degree of

MASTER OF SCIENCE

in

SCIENTIFIC COMPUTING & APPLIED MATHEMATICS

by

**Eonho Chang**

September 2019

The Dissertation of Eonho Chang  
is approved:

---

Professor Qi Gong, Chair

---

Professor Pascale Garaud

---

Professor Nicholas Brummell

---

Professor Dongwook Lee

---

Quentin Williams  
Acting Vice Provost and Dean of Graduate Studies

Copyright © by

Eonho Chang

2019

# Table of Contents

<b>List of Figures</b>	<b>iv</b>
<b>List of Tables</b>	<b>vii</b>
<b>Abstract</b>	<b>viii</b>
<b>Acknowledgments</b>	<b>ix</b>
<b>1 Introduction</b>	<b>1</b>
1.1 Evidence for extra mixing in stars . . . . .	2
1.2 Shear instabilities . . . . .	3
1.3 Adding rotation . . . . .	8
1.4 High-performance computing . . . . .	10
<b>2 Model Setup</b>	<b>12</b>
<b>3 Linear stability analysis</b>	<b>16</b>
3.1 Linearized equations . . . . .	16
3.2 Two remarkable limits . . . . .	19
3.3 Linear stability results . . . . .	23
<b>4 Numerical simulations</b>	<b>27</b>
4.1 Numerical code: PADDI . . . . .	27
4.2 Forcing-based non-dimensionalization . . . . .	27
4.3 Characteristic simulation snapshots . . . . .	29
4.4 Quantitative analysis: mean flow . . . . .	38
4.5 Quantitative analysis: heat transport . . . . .	45
4.6 Quantitative analysis: turbulent momentum transport . . . . .	46
<b>5 Conclusion</b>	<b>51</b>

# List of Figures

2.1 Model setup. . . . .	13
3.1 Linear stability analysis results. White areas are regions that are linearly stable. $\text{Re} = 10^4$ for all maps. From top to bottom: $\text{Pe} = 10^3, 10^2, 10$ . From left to right: growth rate map (log color bar), x-wavenumber map (linear color bar) and y-wavenumber map (log color bar). . . . .	24
4.1 Linear stability analysis results with laminar flow parameters $\text{Re}, \text{Pe}$ and forcing-based parameters $\text{Re}_F, \text{Pe}_F$ . Plotted is the growth rate map (log color bar). Upper: this is the linear stability using the laminar parameters $\text{Re} = 10^4, \text{Pe} = 10^3$ . The green crosses denote the set of parameters with which numerical simulations in Section 4 were run. Lower: this is the linear stability using the turbulent parameters $\text{Re}_F = 10^2, \text{Pe}_F = 0.1$ . The blue crosses denote the predicted locations of the same simulations in the parameter space once turbulence has fully developed. Some of the simulations outside the range are not plotted in the lower panel. . . . .	34

4.2 Characteristic snapshots of flow in the $x$ -direction from simulation data for $\text{Pe}_F = 0.1$ ( $\text{Pe} = 10$ ). From top to bottom: $\text{Ro}_F^{-1} = 40, 5, 0.2$ ( $\text{Ro}^{-1} = 0.4, 0.05, 0.002$ ). From left to right: $\text{Ri}_F = 1, 10, 10^2$ ( $\text{Ri} = 10^{-4}, 10^{-3}, 10^{-2}$ ). The snapshots of simulations with $\text{Ro}_F^{-1} = 1$ ( $\text{Ro}^{-1} = 0.01$ ) are omitted as they looked very similar to those of $\text{Ro}^{-1} = 0.2$ ( $\text{Ro}^{-1} = 0.002$ ) ones. . . . .	35
4.3 Characteristic snapshots of flow in the $y$ -direction from simulation data for $\text{Pe}_F = 0.1$ ( $\text{Pe} = 10$ ). From top to bottom: $\text{Ro}_F^{-1} = 40, 5, 0.2$ ( $\text{Ro}^{-1} = 0.4, 0.05, 0.002$ ). From left to right: $\text{Ri}_F = 1, 10, 10^2$ ( $\text{Ri} = 10^{-4}, 10^{-3}, 10^{-2}$ ). The snapshots of simulations with $\text{Ro}_F^{-1} = 1$ ( $\text{Ro}^{-1} = 0.01$ ) are omitted as they looked very similar to those of $\text{Ro}^{-1} = 0.2$ ( $\text{Ro}^{-1} = 0.002$ ) ones. . . . .	36
4.4 Characteristic snapshots of flow in the $z$ -direction from simulation data for $\text{Pe}_F = 0.1$ ( $\text{Pe} = 10$ ). From top to bottom: $\text{Ro}_F^{-1} = 40, 5, 0.2$ ( $\text{Ro}^{-1} = 0.4, 0.05, 0.002$ ). From left to right: $\text{Ri}_F = 1, 10, 10^2$ ( $\text{Ri} = 10^{-4}, 10^{-3}, 10^{-2}$ ). The snapshots of simulations with $\text{Ro}_F^{-1} = 1$ ( $\text{Ro}^{-1} = 0.01$ ) are omitted as they looked very similar to those of $\text{Ro}^{-1} = 0.2$ ( $\text{Ro}^{-1} = 0.002$ ) ones. . . . .	37
4.5 Mean flow profile in the $x$ -direction from simulation data for $\text{Pe}_F = 0.1$ ( $\text{Pe} = 10$ ). From top to bottom: $\text{Ro}_F^{-1} = 40, 5, 0.2$ ( $\text{Ro}^{-1} = 0.4, 0.05, 0.002$ ). From left to right: $\text{Ri}_F = 1, 10, 10^2, 10^3$ ( $\text{Ri} = 10^{-4}, 10^{-3}, 10^{-2}, 10^{-1}$ ). Each line corresponds to a different snapshot in time. . . . .	39

4.6 Time series of root-mean-square flow amplitudes for the simulation of $\text{Ri}_F = 10, \text{Ro}_F^{-1} = 5$	40
4.7 Time variation of effective system parameters for selected simulations overlaid on the linear stability maps for $\text{Re}_F = 100$ and $\text{Pe}_F = 0.1$ . Crosses in the bottom left corner denote the laminar parameters $\text{Ri}, \text{Ro}^{-1}$ and the ones of the same color in the top right corner denote the forcing- based parameters $\text{Ri}_F, \text{Ro}_F^{-1}$ . The line stretching in between the two crosses correspond to the effective system parameters $\text{Ri}_{\text{eff}}, \text{Ro}_{\text{eff}}^{-1}$	44
4.8 Normalized mean heat flux $\langle wT \rangle / \langle wT \rangle_0$ as a function of the rotation rate $\text{Ro}_F^{-1}$ . Some error bars at $\text{Ro}_F^{-1} = 40$ are greater than the quantity itself in magnitude so that they appear to extend to the bottom of the plot.	46
4.9 $\bar{u}\bar{w}$ vs. $d\bar{u}/dz$ from simulation data for $\text{Pe}_F = 0.1$ ( $\text{Pe} = 10$ ). From top to bottom: $\text{Ro}_F^{-1} = 40, 5, 0.2$ ( $\text{Ro}^{-1} = 0.4, 0.05, 0.002$ ). From left to right: $\text{Ri}_F = 1, 10, 10^2, 10^3$ ( $\text{Ri} = 10^{-4}, 10^{-3}, 10^{-2}, 10^{-1}$ ). Each line corresponds to a different time.	49
4.10 Normalized turbulent viscosity $\nu_{\text{turb}} / \nu_{\text{turb},0}$ as a function of the rotation rate $\text{Ro}_F^{-1}$ . The highest point of the error bar denotes $\nu_- / \nu_{\text{turb},0}$ ; the lowest point of the error bar denotes $\nu_+ / \nu_{\text{turb},0}$	50

# List of Tables

4.1 Simulations and selected quantities. The quantity $\langle wT \rangle$ is discussed in detail in Section 4.5. Note that the ones marked by asterisk * are initialized from the laminar steady state solution $\mathbf{u}(z) = U_L \sin(z)\hat{\mathbf{e}}_x$ . For these ones at least, the initial conditions do not seem to affect simulations in a meaningful way. . . . .	33
4.2 Values of $\nu_{\text{turb}}$ extracted from the simulations. Non-rotating ones are taken from Garaud et al. (2017). Note that $\nu_- = \nu_+$ since the profile is symmetric in the absence of rotation. Also note that generally $\nu_- > \nu_+$ when rotation is present. . . . .	50

## Abstract

Stratified rotational instabilities at low Péclet number

by

Eonho Chang

Observational evidence points to the need for extra mixing in stars. Zahn (1992) proposed a turbulent mixing model due to shear instabilities and the model has been verified to be valid for non-rotating cases. It is not clear, however, whether Zahn's model would still be valid in the presence of rotation. We use a triply-periodic Cartesian domain in the equator of a rotating star to examine this issue. We use the Boussinesq approximation, and assume the background temperature gradient to be constant, and the flow to experience a horizontal sinusoidal body force. A linear stability analysis reveals the existence of several regimes that are dominated by shear instabilities or GSF instabilities. Based on linear stability results, we run a set of numerical simulations for different control parameters including the rotation rate. At small rotation rates, we recover the previous results obtained in the non-rotating case. At higher rotation rates, we find regions governed by different dynamics that are not accounted for by Zahn's model. In each case, we provide quantitative data on the heat and momentum transports induced by turbulence.

## Acknowledgments

The simulations were performed using the PADDI code kindly provided by Stephan Stellmach, on the XSEDE supercomputing facility Comet. This work is funded by NSF-AAG 1814327. I would like to thank Sutirtha Sengupta for his dedicated assistance on producing snapshots of the simulations with VisIt. I also would like to express immense gratitude to my advisor Prof. Pascale Garaud for generously guiding me and helping me correct my mistakes throughout the research, and inviting me to the Geophysical Fluid Dynamics program at the Woods Hole Oceanographic Institution to spend two weeks of productive research.

# Section 1

## Introduction

The theory of stellar evolution attempts to mathematically model the evolution of stars from their birth to their death. The goal of these models is to reproduce the observed physical and chemical state of stars over the course of time. Simple 1D models generally perform well; they fit the most salient aspects of the Hertzsprung-Russel (HR) diagram such as the Hayashi track, the Main Sequence (MS), the Red Giant Branch (RGB), the Horizontal Branch, the existence of White Dwarfs, as well as many other more detailed observations.

Standard stellar models by definition do not include any transport mechanisms beyond convective mixing and associated overshoot. Based on this sole mixing process, the standard theory makes predictions on surface abundances of various chemical elements as well as the evolution of the overall rotational profile. For the most part, observations and standard stellar models do agree with each other. Nevertheless, many discrepancies remain, notably regarding the surface abundances of chemical species such

as Li, Be, B, C, N, O, Fe, Ni, etc.., as well as the differential rotation between the core and envelope in RGB stars. Reconciling the models with observations often requires mixing beyond convective boundaries, whose origin remains to be explained. This is the so-called ‘missing mixing’ problem, and demands additional mechanisms to fill the gap between observation and theory.

## 1.1 Evidence for extra mixing in stars

$^7\text{Li}$  is one of the primordial isotopes produced in the Big Bang, and its abundance is important for studying the Big Bang nucleosynthesis (Olive et al., 2000). Inside stars,  $^7\text{Li}$  is typically destroyed above temperatures of  $\sim 2.5 \times 10^6$  K. Measuring the amount of  $^7\text{Li}$  at the surface and comparing it to the primordial value can help us understand better subsurface stellar mixing through constraints set by  $^7\text{Li}$  depletion.

Indeed, in MS stars, the depth of the surface convection zones is strongly dependent on the mass of the star. Lower mass stars have deeper convection zones that sometimes extend to the core. Close to the core, the base of their convection zones are hot enough to burn light elements like Li on the MS. On the other hand, stars of mass higher than or equal to the Sun’s have shallow and relatively cool surface convection zones, not hot enough to process Li on the MS. Hence, one would expect negligible changes to the surface abundances of light elements in stars with mass  $M > M_\odot$ .

Older solar-type stars, however, are observed to be less abundant in Li than younger ones (Skumanich, 1972; Sestito and Randich, 2005). This strongly suggests

that an extra mixing process other than convection must be at work, that delivers Li from the surface convection zone into the deeper regions of the inner radiative zone where temperatures are high enough to burn Li. The attempt at explaining the surface abundances of light elements dates back to 1951, when Greenstein and Richardson studied the surface abundance of lithium in the Sun and invoked extra mixing as the solution to the problem (Greenstein and Richardson, 1951).

Evidence for extra mixing can also be inferred from the observed differential rotation profile of RGB stars. As stars proceed from the MS to the RGB, their cores shrink and heat up, making their envelopes to inflate. To conserve the angular momentum, the ratio of their core-envelope rotation rate is believed to increase. However, asteroseismological observations show that the models are overestimating the increased ratio by a factor of 10 – 100 (Deheuvels et al., 2012). This implies that the angular momentum transport from the core to the envelope is more efficient than predicted by the models, and hence the need for additional mixing processes in the vicinity of the core-envelope interface.

## 1.2 Shear instabilities

To explain these discrepancies, astrophysicists invoke processes that are not included in standard theory. One of the many possible explanations for the missing mixing comes from shear instabilities caused by differential rotation in the radiative zone.

Linear stability analyses of stratified shear flows have revealed that non-viscous, adiabatic perturbations can only grow if the local Richardson number  $J$  drops below  $1/4$  somewhere in the flow to allow for instability, where:

$$J = \frac{N^2}{S^2}, \quad (1.1)$$

where  $N$  is the Brunt-Väisälä frequency and  $S$  the shearing rate. This criterion is usually referred to as the Richardson criterion (Richardson, 1920), and was formally proven by Miles (1961) and Howard (1961). The criterion can be interpreted energetically: for instability to occur, the kinetic energy extracted by the perturbations from the mean flow, which is proportional to  $S^2$ , must exceed the potential energy lost in mixing the stratified fluid, which is proportional to  $N^2$ .

Townsend (1958) noted that in the presence thermal diffusion, the stabilizing effect of thermal stratification is reduced by the fluid parcel exchanging heat diffusively with its surroundings. For thermal diffusion to be fast enough compared to thermal advection, we need:

$$\mathbf{u} \cdot \nabla T \ll \kappa_T \nabla^2 T, \quad (1.2)$$

where  $\kappa_T$  is the thermal diffusivity. For motion on scale  $l$ , this would dimensionally

correspond to:

$$\frac{UT}{l} \ll \frac{\kappa_T T}{l^2}, \quad (1.3)$$

where  $U$  and  $T$  are characteristic values of the velocity and temperature in the flow.

Equivalently,

$$\frac{Sl^2}{\kappa_T} \ll 1, \quad (1.4)$$

if we take the shear to be  $S = U/l$ . The quantity on the LHS is called the Péclet number  $\text{Pe}_l = Sl^2/\kappa_T$ , and is by definition based on the selected scale  $l$ . Linear stability analysis confirms that when  $\text{Pe}_l$  is much smaller than one, a shear flow with characteristic lengthscale  $l$  is destabilized that otherwise would be stable in the absence of thermal diffusion (Lignières et al., 1999; Garaud et al., 2015).

The Péclet number is related to the Reynolds number  $\text{Re}_l = Ul/\nu = Sl^2/\nu$  by the following:  $\text{Pe}_l = \text{Pr}\text{Re}_l$  where  $\text{Pr} = \nu/\kappa_T$  is the Prandtl number,  $\nu$  being the kinematic viscosity. Because  $\text{Pr}$  is much less than one in stellar interiors, it is plausible for  $\text{Pe}_l$  to be much less than one while  $\text{Re}_l$  remains much larger than one. If  $\text{Re}_l$  were small when  $\text{Pe}_l$  is small, no instability would ensue because of high viscosity. Therefore,  $\text{Pr} \ll 1$  is what makes the diffusive stratified shear instabilities relevant in the context of stellar astrophysics.

Based on Townsend's results, Zahn (1974) proposed the modified stability

criterion suited for stellar interiors:

$$J\text{Pr} < (J\text{Pr})_c, \quad (1.5)$$

where  $(J\text{Pr})_c$  is some constant critical value above which fluid is stable to these diffusive shear instabilities. This implies the stability of a thermally diffusive fluid depends on  $J$ ,  $\text{Pe}$  and  $\text{Re}$ , not just  $J$  as in the Richardson criterion. Zahn estimated the value of the critical Richardson-Prandtl number to be around  $10^{-3}$ . This estimate, when compared with the value of  $\text{Pr} \sim 10^{-5} - 10^{-9}$  in typical stellar interiors suggests that flows with  $J \sim 10^2 - 10^6$  would be unstable, which is within the range of expected Richardson numbers in stars. Under the original Richardson criterion, the same stellar regions would have been thought to be stable.

Later, Zahn (1992) proposed a model for a turbulent mixing coefficient resulting from said diffusive stratified shear instabilities in stellar interiors. His argument starts from a local dimensional analysis, where he postulated that any turbulent diffusion coefficient should take the form:

$$D_{\text{turb}} = \beta S l_e^2, \quad (1.6)$$

where  $l_e$  is the lengthscale of the turbulent eddies and  $\beta$  a constant of order unity. He also argued that the maximum value of  $l_e$  can be derived from the limit of the diffusive

stability criterion such that:

$$J\text{Pe} = (J\text{Pe})_c \implies J \frac{Sl_e^2}{\kappa_T} = (J\text{Pe})_c, \quad (1.7)$$

which gives the value of turbulent eddy scale:

$$l_e = \sqrt{\frac{(J\text{Pe})_c \kappa_T}{JS}}. \quad (1.8)$$

Substituting this into the expression for the turbulent diffusivity gives:

$$D_{\text{turb}} = \beta \frac{(J\text{Pe})_c \kappa_T}{J} = C \frac{\kappa_T}{J}, \quad (1.9)$$

where  $C$  is another constant. Because this derivation comes solely from dimensional arguments, it can be applied to model turbulent transport of any of the quantities such as momentum, angular momentum, or chemical composition.

The two parts of Zahn's proposition have been numerically tested to be valid for non-rotating cases (Prat and Lignières, 2013; Gagnier and Garaud, 2018). Both studies found that Zahn's stability criterion applies with  $(J\text{Pr})_c \approx 0.007$ . They also found that his model for the turbulent diffusivity (and turbulent viscosity) is correct when the turbulence is local and that it fails in the limit of both large and small stratification where locality disappears.

### 1.3 Adding rotation

Although Zahn himself suggested that the results he derived for non-rotating shear flows might be directly applied to flows with rotational shear  $S_\Omega = R d\Omega/dR$ , it is not obvious as there are several complications caused by rotation. One of the effects of rotation is to modify the stability criterion itself. Early studies of rotational shear instabilities were first done by Solberg (1936), Høiland and Bjerknes (1939), and Høiland (1941). In the absence of viscosity and thermal diffusion (i.e. under the same conditions for which the Miles-Howard theorem is valid in the non-rotating case), Solberg and Høiland presented two criteria:

$$\begin{aligned} \frac{1}{R^3} \frac{\partial}{\partial R} (R^4 \Omega^2) - \mathbf{g} \cdot \nabla (\ln \rho) &\leq 0 \text{ or} \\ (\mathbf{g} \cdot \mathbf{e}_\zeta) \left[ \frac{\partial}{\partial R} (R^4 \Omega^2) \frac{\partial}{\partial \zeta} (\ln \rho) - \frac{\partial}{\partial \zeta} (R^4 \Omega^2) \frac{\partial}{\partial R} (\ln \rho) \right] &> 0, \end{aligned} \quad (1.10)$$

where  $\Omega = \Omega(R, \zeta)$  is the angular velocity profile,  $\rho = \rho(R, \zeta)$  the density profile,  $R$  the distance orthogonal to the rotational axis and  $\zeta$  the distance along the rotational axis. Satisfying either of the two criteria implies linear instability. In equatorial regions,  $\mathbf{g} \cdot \mathbf{e}_\zeta = 0$  so the second criterion drops out and the remaining one becomes what is usually known as the Solberg-Høiland criterion:

$$\frac{1}{R^3} \frac{\partial}{\partial R} (R^4 \Omega^2) + N^2 = 2\Omega(2\Omega + S_\Omega) + N^2 \leq 0. \quad (1.11)$$

In the absence of stratification, this criterion recovers the well-known Rayleigh instability criterion for centrifugal instabilities, which states that angular momentum must decrease outward for instability to occur. When stratification is added, we note that the quantity  $N^2/(S\Omega)$  looks similar to the Richardson number  $J = N^2/S^2$  but has a dependency on the sign of the shear. Thus it is clear that the sign of the angular momentum gradient plays a significant role that was absent in the case with linear shear.

Adding the effects of viscosity and thermal diffusion, one arrives at a modified criterion in the equatorial region (Goldreich and Schubert, 1967; Fricke, 1968):

$$\frac{1}{R^3} \frac{\partial}{\partial R} (R^4 \Omega^2) + \frac{\nu}{\kappa_T} N^2 = 2\Omega(2\Omega + S_\Omega) + \text{Pr}N^2 \leq 0. \quad (1.12)$$

which reveals the dependence on  $\text{Pr}$ . This is known as the Goldreich-Schubert-Fricke stability (GSF) criterion, and instabilities that arise when it is broken are usually called GSF instabilities. We see that for a sufficiently small value of  $\text{Pr}$ , which is the case in stellar interiors, the effect of stratification can be neglected. In that case, we simply recover Rayleigh's criterion for centrifugal instabilities once again.

As can be seen from the above two criteria, rotational instabilities fundamentally differ from their non-rotational counterparts. As a result, strong doubts should exist as to the applicability of Zahn's model to rotational shear.

## 1.4 High-performance computing

As powerful supercomputing clusters have become available, the validity of Zahn’s theory can now be verified through numerical experiments using high-performance computing.

Unfortunately, however, a comprehensive study of all possible fluid dynamical processes in stellar interiors still remains far from reach due to the immense range of scales involved in both large-scale flows and small-scale turbulence. Furthermore, these local simulations cannot be run at actual stellar parameters due to computational constraints (i.e.  $\text{Pr} \ll 1$  and  $\text{Re} \gg 1$ ). Only by considering very idealized conditions and making additional simplifications can we create a model setup that can be studied using Direct Numerical Simulations.

As such, the goal of numerical simulations is not to reproduce the exact same conditions as real stars, but to understand how individual transport processes depend on input parameters such as the viscosity, diffusivity, ambient stratification, and local shear, first qualitatively, and then quantitatively. Any insight into the missing mixing problem from these idealized simulations will help understand better the stellar transport processes and benefit future studies on this subject. In this work, we set out to verify the validity of Zahn’s mixing model with rotation in consideration. In the section to follow we discuss the model setup and equations that describe it. In Section 3, linearized equations and analysis of the model system are presented. In Section 4, results of the numerical investigation are discussed. Finally, in Section 5, we summarize the

work done, and discuss implications of the results and future directions.

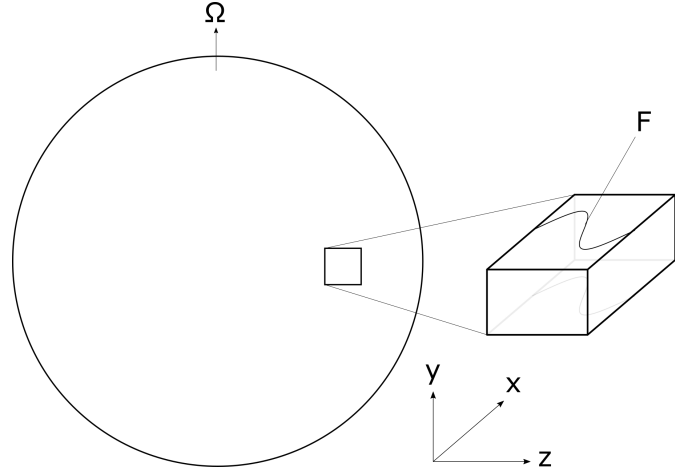
## Section 2

### Model Setup

We consider a Cartesian box at the equator of a star rotating with a constant angular velocity  $\Omega = \Omega_0$ . We label the axes such that  $y$  is the axis of rotation,  $z$  marks the local vertical which corresponds to the radial direction, and  $x$  is one of the azimuthal directions that makes the system right-handed.

Assuming that the domain size is smaller than any of the local scaleheights, we use the Boussinesq approximation (Spiegel and Veronis, 1960) and neglect the effect of compositional stratification. We then linearize the background thermal stratification around the mean temperature in the  $z$  direction as  $T_0(z) = T_m + zT_{0z}$ . The domain is assumed to be periodic in each of the directions. Also present in the box is a sinusoidal shear driven by a body force in the  $x$ -direction  $\mathbf{F} = F_0 \sin(k_s z) \hat{\mathbf{e}}_x$ , where  $F_0$  is the amplitude of the shear and  $k_s$  is the wavenumber in the  $z$ -direction.

Figure 2.1: Model setup.



The following dimensional equations govern the dynamics of the model described above:

$$\begin{aligned} \rho_m \left( \frac{\partial \mathbf{u}}{\partial t} + \mathbf{u} \cdot \nabla \mathbf{u} + 2\Omega_0 \times \mathbf{u} \right) &= -\nabla p + \rho g + \rho_m \nu \nabla^2 \mathbf{u} + F_0 \sin(k_s z) \hat{\mathbf{e}}_x, \\ \frac{\partial T}{\partial t} + \mathbf{u} \cdot \nabla T + w \left( T_{0z} - \frac{dT_{\text{ad}}}{dz} \right) &= \kappa_T \nabla^2 T, \end{aligned} \quad (2.1)$$

$$\nabla \cdot \mathbf{u} = 0,$$

$$\frac{\rho}{\rho_m} = -\alpha T,$$

where  $p$  and  $T$  are the pressure and temperature perturbations away from the background quantities,  $\rho_m$  is the mean density of the region considered, and  $\mathbf{u} = (u, v, w)$  is the velocity field. We assume kinematic viscosity  $\nu$ , thermal diffusivity  $\kappa_T$ , the local gravity  $g$ , and the thermal expansion coefficient  $\alpha = -\rho_m^{-1}(\partial\rho/\partial T)$  to be constants.

Because of the imposed sinusoidal forcing, the system has a laminar steady

state solution given by:

$$\mathbf{u}_L = \frac{F_0}{\rho_m \nu k_s^2} \sin(k_s z) \hat{\mathbf{e}}_x. \quad (2.2)$$

and we can non-dimensionalize the above equations using the amplitude of the laminar solution  $U_L = F_0 / (\rho_m \nu k_s^2)$  as a velocity scale, and the spatial scale of the laminar solution  $k_s^{-1}$  as a lengthscale. The corresponding non-dimensional equations are:

$$\begin{aligned} \frac{D\tilde{\mathbf{u}}}{Dt} &= -\nabla \tilde{p} + \text{Ri} \tilde{T} \hat{\mathbf{e}}_z + \frac{1}{\text{Re}} \nabla^2 \tilde{\mathbf{u}} - \frac{\tilde{w}}{\text{Ro}} \hat{\mathbf{e}}_x + \frac{\tilde{u}}{\text{Ro}} \hat{\mathbf{e}}_z + \sin \tilde{z} \hat{\mathbf{e}}_x, \\ \frac{\partial \tilde{T}}{\partial \tilde{t}} + \tilde{\mathbf{u}} \cdot \nabla \tilde{T} + \tilde{w} &= \frac{1}{\text{Pe}} \nabla^2 \tilde{T}, \\ \nabla \cdot \tilde{\mathbf{u}} &= 0, \end{aligned} \quad (2.3)$$

where the independent variables have been non-dimensionalized, and where tildes denote non-dimensional dependent variables, with the following dimensionless parameters:

$$\begin{aligned} \text{Re} &= \frac{U_L}{k_s \nu} = \frac{F_0}{\rho_m \nu^2 k_s^3}, \\ \text{Ri} &= \frac{N^2}{U_L^2 k_s^2} = \frac{\alpha g T_{0z} \rho_m^2 \nu^2 k_s^2}{F_0^2}, \\ \text{Pe} &= \frac{U_L}{k_s \kappa_T} = \frac{F_0}{\rho_m \nu k_s^3 \kappa_T}, \\ \text{Ro} &= \frac{k_s U_L}{2\Omega_0} = \frac{F_0}{2\Omega_0 \rho_m \nu k_s}. \end{aligned} \quad (2.4)$$

The Reynolds number  $\text{Re}$  quantifies the ratio of the viscous diffusion timescale to the turbulent turnover timescale. The Richardson number  $\text{Ri}$  is the square of the ratio of the buoyancy frequency to the maximum shearing rate, which is used as a proxy for

quantifying the potential energy lost in mixing the stratification to the kinetic energy gained from the shear. The Péclet number  $\text{Pe}$  is the ratio of the thermal diffusion timescale to the turbulent turnover timescale. Finally, the Rossby number  $\text{Ro}$  is the ratio of the mean shearing rate to the rotation rate which measures the relative importance of the inertial force and the Coriolis force.

## Section 3

### Linear stability analysis

#### 3.1 Linearized equations

In this section, we look at the stability of the laminar steady state solution. We consider 3D infinitesimal perturbations (denoted by the primes) such that  $\tilde{\mathbf{u}} = \tilde{\mathbf{u}}_L + \tilde{\mathbf{u}}'$ . The linearization of Eqns. 2.3 results in:

$$\begin{aligned} \frac{\partial \tilde{\mathbf{u}}'}{\partial \tilde{t}} + \tilde{\mathbf{u}}_L \cdot \nabla \tilde{\mathbf{u}}' + \tilde{\mathbf{u}}' \cdot \nabla \tilde{\mathbf{u}}_L &= -\nabla \tilde{p}' + \text{Ri} \tilde{T}' \hat{\mathbf{e}}_z + \frac{1}{\text{Re}} \nabla^2 \tilde{\mathbf{u}}' - \frac{\tilde{w}'}{\text{Ro}} \hat{\mathbf{e}}_x + \frac{\tilde{u}'}{\text{Ro}} \hat{\mathbf{e}}_z, \\ \frac{\partial \tilde{T}'}{\partial \tilde{t}} + \tilde{\mathbf{u}}_L \cdot \nabla \tilde{T}' + \tilde{w}' &= \frac{1}{\text{Pe}} \nabla^2 \tilde{T}', \\ \nabla \cdot \tilde{\mathbf{u}}' &= 0, \end{aligned} \tag{3.1}$$

where  $\tilde{p}'$  and  $\tilde{T}'$  are assumed to be small. The linearized equations in component form are:

$$\begin{aligned} \frac{\partial u'}{\partial t} + w' \frac{du_L}{dz} + u_L \frac{\partial u'}{\partial x} &= -\frac{\partial p'}{\partial x} + \frac{1}{Re} \nabla^2 u' - \frac{w'}{Ro}, \\ \frac{\partial v'}{\partial t} + u_L \frac{\partial v'}{\partial x} &= -\frac{\partial p'}{\partial y} + \frac{1}{Re} \nabla^2 v', \\ \frac{\partial w'}{\partial t} + u_L \frac{\partial w'}{\partial x} &= -\frac{\partial p'}{\partial z} + Ri T' + \frac{1}{Re} \nabla^2 w' + \frac{u'}{Ro}, \\ \frac{\partial T'}{\partial t} + u_L \frac{\partial T'}{\partial x} + w' &= \frac{1}{Pe} \nabla^2 T', \\ \frac{\partial u'}{\partial x} + \frac{\partial v'}{\partial y} + \frac{\partial w'}{\partial z} &= 0, \end{aligned} \quad (3.2)$$

where the tildes have now been dropped for readability. From this point until the end of the section, all quantities may be assumed non-dimensionalized unless mentioned otherwise.

The system of Eqns. 3.2 has non-constant coefficients, since  $u_L$  and its derivative are periodic functions of  $z$ . Nevertheless, using Floquet theory, they can be turned into a system of linear algebraic equations. We do so first by assuming that perturbation quantities  $q'(x, y, z, t)$  can be written as normal modes:

$$q'(x, y, z, t) = \hat{q}(z) \exp(ik_x x + ik_y y + \lambda t), \quad (3.3)$$

where  $q'$  can be either  $\mathbf{u}'$ ,  $T'$  or  $p'$ ,  $k_x$  and  $k_y$  are the wave numbers in  $x$  and  $y$  respectively, and  $\lambda$  is a complex growth rate. Since the laminar steady state solution  $\mathbf{u}_L = \sin(z)\hat{\mathbf{e}}_x$

is periodic in  $z$ , we similarly seek solutions of the form:

$$\hat{q}(z) = \sum_{n=-\infty}^{\infty} q_n \exp(inz). \quad (3.4)$$

Substituting these ansätze into the linearized equations, we obtain a system of algebraic equations for the Fourier coefficients  $q_n$ :

$$\begin{aligned} \lambda u_n + \frac{w_{n-1}}{2} + \frac{w_{n+1}}{2} + \frac{k_x u_{n-1}}{2} - \frac{k_x u_{n+1}}{2} &= -ik_x p_n - \text{Re}^{-1} |\mathbf{k}|^2 u_n - \text{Ro}^{-1} w_n, \\ \lambda v_n + \frac{k_x v_{n-1}}{2} - \frac{k_x v_{n+1}}{2} &= -ik_y p_n - \text{Re}^{-1} |\mathbf{k}|^2 v_n, \\ \lambda w_n + \frac{k_x w_{n-1}}{2} - \frac{k_x w_{n+1}}{2} &= -inp_n + \text{RiT}_n - \text{Re}^{-1} |\mathbf{k}|^2 w_n + \text{Ro}^{-1} u_n, \\ \lambda T_n + \frac{k_x T_{n-1}}{2} - \frac{k_x T_{n+1}}{2} + w_n &= -\text{Pe}^{-1} |\mathbf{k}|^2 T_n, \\ k_x u_n + k_y v_n + n w_n &= 0, \end{aligned} \quad (3.5)$$

where  $\mathbf{k} = (k_x, k_y, n)$ . This can be cast as a generalized eigenvalue/vector problem:

$$\mathbf{M}(\mathbf{k}, \text{Re}, \text{Ri}, \text{Pe}, \text{Ro})\mathbf{x} = \lambda \mathbf{x}, \quad (3.6)$$

where  $\mathbf{x} = (u_{-N}, \dots, u_N, v_{-N}, \dots, v_N, \dots, T_{-N}, \dots, T_N)$  is the solution vector for some finite  $N$ . The size of the system can be reduced by eliminating the pressure  $p_n$  and the

flow in  $y$ -direction  $v_n$  analytically:

$$\begin{aligned}
\lambda u_n + \frac{w_{n-1}}{2} + \frac{w_{n+1}}{2} + \frac{k_x u_{n-1}}{2} - \frac{k_x u_{n+1}}{2} &= -ik_x p_n - \text{Re}^{-1} |\mathbf{k}|^2 u_n - \text{Ro}^{-1} w_n, \\
\lambda w_n + \frac{k_x w_{n-1}}{2} - \frac{k_x w_{n+1}}{2} &= \text{RiT}_n - \text{Re}^{-1} |\mathbf{k}|^2 w_n + \text{Ro}^{-1} u_n \\
&\quad - \frac{n}{k_y^2} \left[ (\lambda + \text{Re}^{-1} |\mathbf{k}|^2) (k_x u_n + n w_n) + \frac{k_x}{2} \{k_x (u_{n-1} - u_{n+1}) + n (w_{n-1} - w_{n+1})\} \right], \\
\lambda T_n + \frac{k_x T_{n-1}}{2} - \frac{k_x T_{n+1}}{2} + w_n &= -\text{Pe}^{-1} |\mathbf{k}|^2 T_n.
\end{aligned} \tag{3.7}$$

Then the system can be numerically solved for  $\lambda$  to understand the linear stability for a given set of parameters  $\text{Re}$ ,  $\text{Ri}$ ,  $\text{Pe}$  and  $\text{Ro}$ , and selected wavenumber  $\mathbf{k}$ .

### 3.2 Two remarkable limits

Although we generally need to solve the system numerically, two remarkable limits can be obtained analytically from Eqns. 3.2. The first limit is obtained assuming invariance in the  $y$ -direction. Then, by definition, the derivative  $\partial/\partial y$  of any quantity drops out from the equations. For instance, the incompressibility equation reduces to:

$$\frac{\partial u'}{\partial x} + \frac{\partial w'}{\partial z} = 0. \tag{3.8}$$

By taking the  $z$ -derivative of the  $x$ -momentum equation and the  $x$ -derivative

of the  $z$ -momentum equation, one arrives at the following two equations:

$$\begin{aligned}\frac{\partial}{\partial z} \left( \frac{\partial u'}{\partial t} + w' \frac{du_L}{dz} + u_L \frac{\partial u'}{\partial x} \right) &= \frac{\partial}{\partial z} \left( -\frac{\partial p'}{\partial x} + \frac{1}{\text{Re}} \nabla^2 u' \right) - \frac{1}{\text{Ro}} \frac{\partial w'}, \\ \frac{\partial}{\partial x} \left( \frac{\partial w'}{\partial t} + u_L \frac{\partial w'}{\partial x} \right) &= \frac{\partial}{\partial x} \left( -\frac{\partial p'}{\partial z} + \text{Ri} T' + \frac{1}{\text{Re}} \nabla^2 w' \right) + \frac{1}{\text{Ro}} \frac{\partial u'}{\partial z}.\end{aligned}\quad (3.9)$$

We note that these two are the only equations directly affected by rotation. If we subtract one from the other, with the new incompressibility condition (Eqn. 3.8), terms containing  $\text{Ro}$  entirely disappear from the system to yield,

$$\begin{aligned}\frac{\partial}{\partial t} \left( \frac{\partial u'}{\partial z} - \frac{\partial w'}{\partial x} \right) + \left( \frac{\partial}{\partial z} \left( u_L \frac{\partial u'}{\partial x} \right) - u_L \frac{\partial^2 w'}{\partial x^2} \right) + \frac{\partial}{\partial z} \left( w' \frac{du_L}{dz} \right) \\ = -\text{Ri} \frac{\partial T'}{\partial x} + \frac{1}{\text{Re}} \nabla^2 \left( \frac{\partial u'}{\partial z} - \frac{\partial w'}{\partial x} \right).\end{aligned}\quad (3.10)$$

This shows that rotation has no effect on the linear evolution of  $y$ -invariant perturbations in the equatorial regions of a star. Hence, we expect to recover the stability properties of standard diffusive stratified shear instabilities for  $k_y = 0$  modes, regardless of the rotation rate.

On the other hand, if we assume  $x$ -invariance ( $\partial/\partial x = 0$ ), all the advection terms as well as other derivatives in  $x$  drop out from the equations to give the following

set of PDE's:

$$\begin{aligned}
\frac{\partial u'}{\partial t} + w' \frac{du_L}{dz} &= \frac{1}{\text{Re}} \nabla^2 u' - \frac{w'}{\text{Ro}}, \\
\frac{\partial v'}{\partial t} &= -\frac{\partial p'}{\partial y} + \frac{1}{\text{Re}} \nabla^2 v', \\
\frac{\partial w'}{\partial t} &= -\frac{\partial p'}{\partial z} + \text{RiT}' + \frac{1}{\text{Re}} \nabla^2 w' + \frac{u'}{\text{Ro}}, \\
\frac{\partial T'}{\partial t} + w' &= \frac{1}{\text{Pe}} \nabla^2 T', \\
\frac{\partial v'}{\partial y} + \frac{\partial w'}{\partial z} &= 0.
\end{aligned} \tag{3.11}$$

For the moment, we further assume constant shear of  $\mathcal{S} = du_L/dz$ . Then the system becomes autonomous, and we can eliminate variables to arrive at the following equation:

$$D_{\mathbf{u}}^2 D_T \nabla^2 w' = \left[ \frac{1}{\text{Ro}} D_T \left( \frac{1}{\text{Ro}} + \mathcal{S} \right) - \text{Ri} D_{\mathbf{u}} \right] \frac{\partial^2 w'}{\partial y^2}, \tag{3.12}$$

where  $D$ 's are shorthand notations for differential operators:

$$D_{\mathbf{u}} = \frac{1}{\text{Re}} \nabla^2 - \frac{\partial}{\partial t}, \quad D_T = \frac{1}{\text{Pe}} \nabla^2 - \frac{\partial}{\partial t}. \tag{3.13}$$

We assume simple normal mode solutions of the form  $w' \propto \exp(ik_y y + ik_z z + \lambda t)$  and obtain the algebraic equation:

$$\left( \frac{K^2}{\text{Re}} + \lambda \right)^2 \left( \frac{K^2}{\text{Pe}} + \lambda \right) K^2 = \left[ \frac{1}{\text{Ro}} \left( \frac{K^2}{\text{Pe}} + \lambda \right) \left( \frac{1}{\text{Ro}} + \mathcal{S} \right) - \text{Ri} \left( \frac{K^2}{\text{Re}} + \lambda \right) \right] k_y^2, \tag{3.14}$$

where  $K^2 = k_y^2 + k_z^2$ . This can be expanded to give a third order polynomial equation in  $\lambda$ :

$$\begin{aligned} \lambda^3 + a_2\lambda^2 + a_1\lambda + a_0 &= 0, \\ a_2 &= \left( \frac{1}{Pe} + \frac{2}{Re} \right) K^2, \\ a_1 &= \left( \frac{2}{RePe} + \frac{1}{Re^2} \right) K^4 + Ri \frac{k_y^2}{K^2} - \frac{1}{Ro} \left( \frac{1}{Ro} + S \right) \frac{k_y^2}{K^2}, \\ a_0 &= \frac{K^6}{Re^2Pe} + Ri \frac{k_y^2}{Re} - \frac{k_y^2}{RoRe} \left( \frac{1}{Ro} + S \right). \end{aligned} \tag{3.15}$$

The absence of any solution with positive real part (which is necessary for stability) can be established using the Routh-Hurwitz theorem. For a third order polynomial, the Routh-Hurwitz stability criterion is satisfied if and only if  $a_2, a_0 > 0$  and  $a_2a_1 > a_0$  (Anagnos and Desoer, 1991). Specifically, the condition  $a_0 > 0$  gives the following inequality:

$$\frac{1}{Re^2} \frac{K^6}{k_y^2} > \frac{1}{Ro} \left( \frac{1}{Ro} + S \right) - RiPr. \tag{3.16}$$

For this to be true for any value of  $k_y, k_z \neq 0$ , the RHS must be non-positive:

$$0 \geq \frac{1}{Ro} \left( \frac{1}{Ro} + S \right) - RiPr. \tag{3.17}$$

This is equivalent to the non-dimensional version of the GSF stability criterion in Eqn. 1.12. We now have analytically identified two distinct modes of instability, one with  $k_y = 0$  that does not know about rotation, and one with  $k_x = 0$  which is the standard

GSF instability (see above).

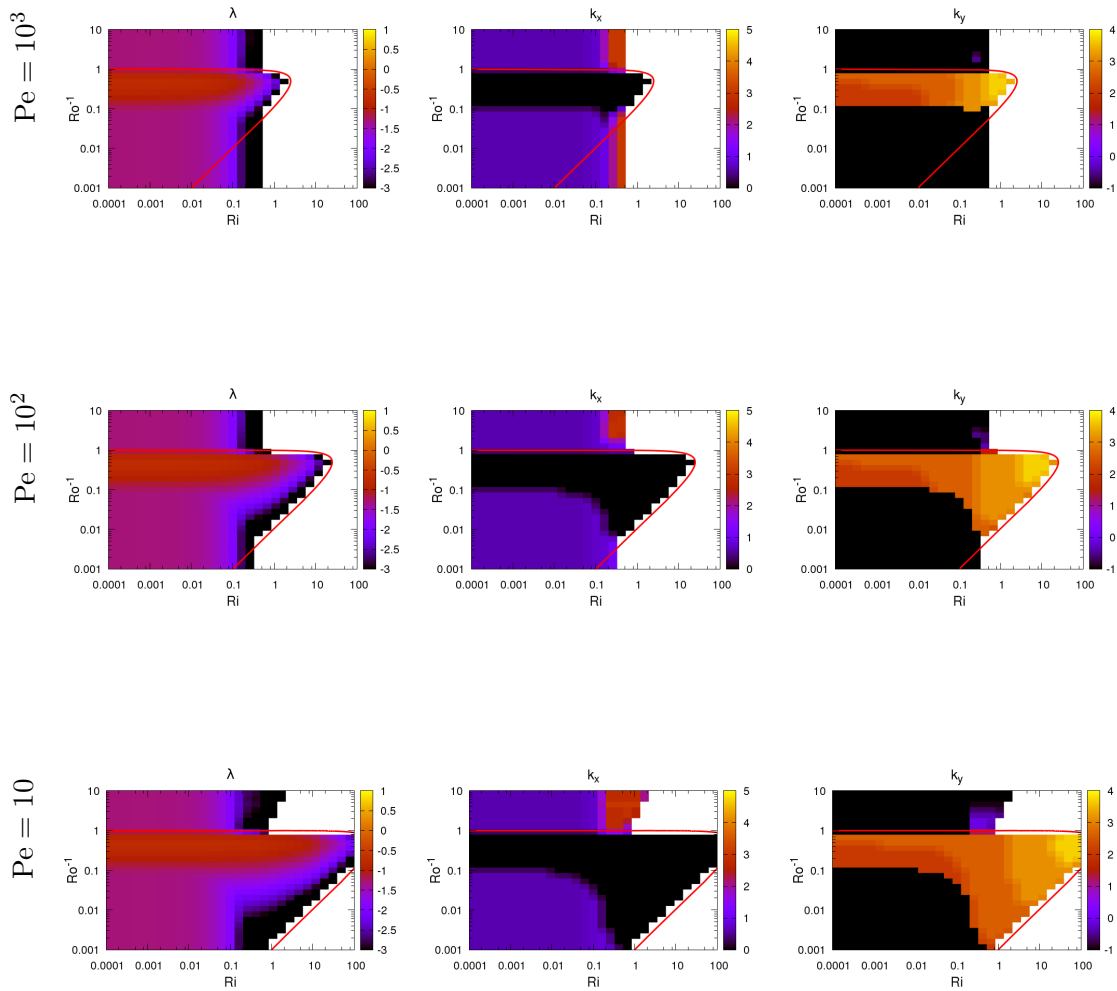
### 3.3 Linear stability results

The reduced system of Eqns. 3.7 was solved by numerically searching for the fastest growing modes for each set of  $\text{Ro}^{-1}$  and  $\text{Ri}$ . Fig. 3.1 shows the corresponding linear stability maps in  $\text{Ro}^{-1} \in [10^{-3}, 10]$  and  $\text{Ri} \in [10^{-4}, 10^2]$  for various values of  $\text{Pe} = 10^3, 10^2, 10$  and a fixed value of  $\text{Re} = 10^4$ . The inverse Rossby number  $\text{Ro}^{-1}$  is proportional to the rotation rate as can be seen in Eqn. 2.4.

For non-rotating or very weakly rotating limit, ( $\text{Ro}^{-1} \in [0, 10^{-2}]$ ), we can see from Fig. 3.1 that the neutral stability line lies close to one, even for large Péclet number. This may seem surprising at first given that the Richardson criterion states that stratified shear flows are linearly stable if the gradient Richardson number, which is equal to  $J = \text{Ri}/\cos^2(z)$  in this problem, is greater than  $1/4$  everywhere in the flow, which happens as soon as  $\text{Ri} > 1/4$ . This is due to the fact that the standard Richardson criterion neglects viscous effects, and thus fails to capture the viscosity-driven instabilities. Between  $\text{Ri} = 1/4$  and  $\text{Ri} = 1$ , viscous modes exist and can be distinguished by their small growth rates. This has been shown by Balmforth and Young (2002) in the case of stratified 2D sinusoidal shear flows and Garaud et al. (2015) in the case of stratified 3D sinusoidal shear flows.

As  $\text{Pe}$  decreases, we also see that instabilities can exist at higher Richardson numbers. Since the inverse of the Péclet number  $\text{Pe}^{-1}$  represents how thermally diffusive

Figure 3.1: Linear stability analysis results. White areas are regions that are linearly stable.  $Re = 10^4$  for all maps. From top to bottom:  $Pe = 10^3, 10^2, 10$ . From left to right: growth rate map (log color bar), x-wavenumber map (linear color bar) and y-wavenumber map (log color bar).



the system is, decreasing Pe is equivalent to increasing thermal diffusion in the system. Faster thermal diffusion acts as a destabilizing agent against the density stratification, allowing for the existence of unstable modes at higher values of Ri. In the very weakly rotating limit, our result therefore recovers that of Townsend (1958).

As we increase the rotation rate (by increasing the value of  $\text{Ro}^{-1}$ ), we see the emergence of several regions of parameter space with distinct stability properties. In the weakly rotating region, roughly corresponding to  $\text{Ro}^{-1} \in [10^{-2}, 10^{-1}]$ , the dominant mode of instability is primarily 2D, with  $k_y = 0$ , and is therefore independent of  $\text{Ro}^{-1}$  as discussed in Section 3.2. In this region of  $k_y = 0$ , the system is negligibly affected by rotation, and thus linearly unstable to the familiar diffusive stratified shear instabilities. For intermediate rotation rates, roughly corresponding to the interval  $\text{Ro}^{-1} \in [10^{-1}, 1]$ , the dominant instabilities change from  $y$ -invariant modes to favor axisymmetric modes with  $k_x = 0$ . These modes are the GSF modes discussed in Section 3.2. This transition suggests that rotation starts to take effect and alter the dynamics significantly. Moving on to the region with higher rotation rates ( $\text{Ro}^{-1} > 1$ ), we see the dominant mode is the one with  $k_y = 0$  again. Hence we recover the original shearing mode we saw at lower rotation rates.

The solution of Eqn. 3.17 is drawn to identify the region subject to GSF instabilities, as the red curve in Fig. 3.1. The system is susceptible to GSF instabilities according to the criterion, to the left and below the red curve, at values of  $\text{Ro}^{-1} \lesssim 1$ . We see that the criterion correctly identifies the upper and rightmost edge of the “wedge”-shaped GSF instability region of the parameter space. However we also see that the

GSF modes are not the fastest-growing ones at lower rotation rates, where the shearing modes dominate.

As  $\text{Pe}$  decreases, the GSF “wedge” expands to encompass higher  $\text{Ri}$  values and lower rotation rates, consistent with the criterion in Eqn. 3.17. Similarly to the non-rotating limit, as  $\text{Pe}$  decreases thermal diffusion becomes important. In the presence of significant thermal diffusion, the stabilizing effect of stratification becomes weaker and this facilitates the effect of rotation to take over. Hence, a larger portion of the map is susceptible to rotational instabilities.

Finally, we see that as  $\text{Ri}$  increases, the  $y$ -wavenumber of fastest growing GSF modes also tends to increase in the “wedge”. This is due to the fact that the GSF instabilities are analogous to double diffusive fingering instabilities whose characteristic lengthscale is proportional to  $\text{Ra}^{-1/4}$  (Barker et al., 2019). Because the Rayleigh number is expressed as  $\text{Ra} = \text{PeReRi}$  in this model, an increase in  $\text{Ri}$  will translate into a decrease in the characteristic lengthscale, and therefore increase in the characteristic wavenumber of the fastest growing mode.

## Section 4

# Numerical simulations

In what follows, we now turn to numerical simulations to study the nonlinear aspects of the instabilities in rotating diffusive stratified shear flows.

### 4.1 Numerical code: PADDI

PADDI is a high-performance pseudo-spectral code originally developed to solve double-diffusive hydrodynamic equations over a triply-periodic 3D domain by Traxler et al. (2011) and Stellmach et al. (2011). The original code has been modified to include both the Coriolis force (as in Moll and Garaud 2017; Sengupta and Garaud 2018) and the sinusoidal body force (as in Garaud et al. 2017; Kulenthirarajah and Garaud 2018) to suit the needs of the study.

### 4.2 Forcing-based non-dimensionalization

For the purpose of the linear stability analysis in Section 3, we employed a non-dimensionalization based on the amplitude of the laminar steady state solution:  $U_L = F_0/(\rho_m \nu k^2)$ . An alternative way of non-dimensionalizing the equations comes from using a velocity scale based on the forcing. For turbulent simulations with low or moderate rotation rates, we expect that the inertial term and the forcing are in an approximate balance such that:

$$\rho_m (\mathbf{u} \cdot \nabla \mathbf{u}) \cdot \hat{\mathbf{e}}_x \sim F_0, \quad (4.1)$$

in the dimensional momentum equation. Then we can define a new flow amplitude  $U_F$  as:

$$U_F = \left( \frac{F_0}{k_s \rho_m} \right)^{1/2}, \quad (4.2)$$

(see Garaud and Kulenthirarajah 2016, for instance). This velocity scale is not sensitive to any diffusivity, and thus it is more relevant than  $U_L$  once turbulence has fully developed. In this new system of units, we have the parameters:

$$\begin{aligned} \text{Re}_F &= \frac{U_F}{k_s \nu} = \left( \frac{F_0}{\rho_m \nu^2 k_s^3} \right)^{1/2} = \text{Re}^{1/2}, \\ \text{Ri}_F &= \frac{N^2}{U_F^2 k_s^2} = \frac{N^2 \rho_m}{k_s F_0} = \text{ReRi}, \\ \text{Pe}_F &= \frac{U_F}{k_s \kappa_T} = \left( \frac{F_0}{\rho_m \nu k_s^3 \kappa_T^2} \right)^{1/2} = \text{Re}^{-1/2} \text{Pe}, \\ \text{Ro}_F &= \frac{k_s U_F}{2\Omega_0} = \left( \frac{k_s F_0}{4\Omega_0^2 \rho_m} \right)^{1/2} = \text{Re}^{-1/2} \text{Ro}. \end{aligned} \quad (4.3)$$

As demonstrated by Garaud and Kulenthirarajah (2016), these are good estimates for the actual turbulent Reynolds, Péclet and Richardson numbers in non-rotating stratified shear flows. We will now determine whether they, together with the Rossby number  $\text{Ro}_F$ , are also good estimates for the turbulent parameters in the rotating case.

### 4.3 Characteristic simulation snapshots

In this section we present a few characteristic snapshots of simulations to illustrate the typical results we have obtained at low Péclet number. Tab. 4.1 lists all of the simulation runs and measured quantities. Figs. 4.2-4.4 show characteristic snapshots of simulations in their respective statistically steady states.

We picked three sets of values of  $\text{Ri}$ , and four sets of values of  $\text{Ro}^{-1}$ , shown as the green crosses in Fig. 4.1a. While these appear to mostly span the “shear-unstable” region of parameter space, with only a few in the GSF “wedge”, we will demonstrate below that the nonlinear development of the instability strongly modifies the mean flow, so the effective Richardson, Reynolds, Péclet and Rossby numbers are quite different from their laminar counterpart. As a result, the actual system dynamics in the turbulent flow are quite different from those anticipated by the linear stability analysis applied to the laminar flow. In addition to the 12 simulations, we added another one to explore interesting region of parameter space based on the linear stability analysis. We have run a total of 13 simulations at  $\text{Pe}_F = 0.1$ .

To select the values of  $\text{Ri}_F$  and  $\text{Ro}_F$  for our simulations, note that a better

estimate of the position of our simulations in parameter space can be obtained by redoing a linear stability analysis of the system but this time using the anticipated turbulent mean flow amplitude  $U_F$  instead of  $U_L$ . To do so, we simply replace  $\text{Re}$ ,  $\text{Pe}$ ,  $\text{Ro}$  and  $\text{Ri}$  in Eqn. 2.4 by their corresponding values of  $\text{Re}_F$ ,  $\text{Pe}_F$ ,  $\text{Ro}_F$  and  $\text{Ri}_F$ , using the relationships given in Eqn. 4.3. The resulting linear stability plot is shown in Fig. 4.1b, and the blue crosses are the positions of our simulations. We see that they now span a variety of conditions, including shear unstable, GSF unstable, rotationally dominated, and even some taken in the stable region of parameter space. Note that the position of the blue crosses is again merely indicative of the expected dynamics since the actual amplitude of the mean flow could differ from  $U_F$ . In Section 4.4, we compute the mean flow to better estimate the effective Richardson, Reynolds, Péclet and Rossby numbers of the flow.

Simulations are either initialized from small random perturbations to the laminar solution, or from the endpoint of another simulation ran at slightly different input parameters. The ultimate statistically stationary state reached by the system seems to be independent of the initial conditions (at least, it is in all the cases for which both sets of initial conditions were tested).

In the weakly rotating simulations with  $\text{Ro}_F^{-1} = 0.2$  (which correspond to  $\text{Ro}^{-1} = 2 \times 10^{-3}$ ), the effect of rotation is negligible and we recover results very similar to those obtained by Garaud and Kulenthirarajah (2016). In Fig. 4.2, we see that as the Richardson number increases from the weakly stratified limit  $\text{Ri}_F = 1$  (i.e.  $\text{Ri} = 10^{-4}$ ) to what they refer to as the strongly stratified limit  $\text{Ri}_F = 10^2$  (i.e.  $\text{Ri} = 10^{-2}$ ) the

mean flow becomes apparent. At the same time, Fig. 4.4 shows that the scale of vertical velocity fluctuations decreases as stratification increases. This is because smaller eddy scales result in a lower potential energy cost for each turnover at higher  $\text{Ri}_F$ . Smaller scales allow for faster diffusion, which translates into smaller differences in temperature and thus in density. Smaller density differences incur a smaller potential energy cost, and hence smaller eddy scales are favored over larger ones. Because the smaller eddy scales imply strong thermal diffusion, Eqn. 1.8 gives the largest eddy scale where Eqn. 1.7 holds true in Zahn's model. At the same time, according to Eqn. 1.6, smaller eddy scales imply a decrease in the turbulent viscosity and this in turn results in the increase of the amplitude of the mean flow. This is in agreement with previous results (Garaud and Kulenthirarajah 2016; Garaud et al. 2017).

Interestingly, at the rotation rate of  $\text{Ro}_F^{-1} = 1$  ( $\text{Ro}^{-1} = 10^{-2}$ ), we observe a transition between the weakly rotating limit and the regime non-negligibly affected by rotation. For weaker stratification values, the snapshots of  $\text{Ro}_F^{-1} = 0.2$  and  $\text{Ro}_F^{-1} = 1$  look alike whereas in the strongly stratified limit, those of  $\text{Ro}_F^{-1} = 1$  and  $\text{Ro}_F^{-1} = 5$  look very similar.

As we increase  $\text{Ro}_F^{-1}$ , the effect of rotation becomes visible in Figs. 4.2 and 4.4. For an intermediate rotation rate  $\text{Ro}_F^{-1} = 5$  ( $\text{Ro}^{-1} = 5 \times 10^{-2}$ ), the more weakly stratified simulation ( $\text{Ri}_F = 1$ ) shows roll-like structures invariant in the  $y$ -direction. However, this is only true for low values of  $\text{Ri}_F$ , and as  $\text{Ri}_F$  increases, the flow becomes 3D again. In the strongly stratified limit, we see from snapshots of the vertical velocity that turbulence is limited to the middle of the domain (where  $S < 0$ ) and is almost

nonexistent at the top and the bottom of the domain (where  $S > 0$ ). This asymmetry suggests that centrifugal instabilities may be at play since the GSF stability criterion depends on the sign of the shear (Eqn. 3.17). Specifically,  $S < 0$  is destabilizing and  $S > 0$  is stabilizing, which is consistent with our numerical findings.

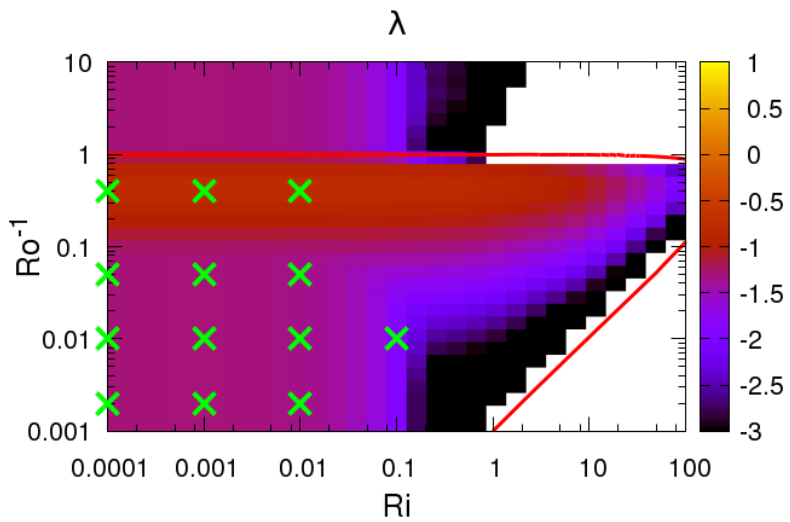
As we reach the higher rotation rate of  $\text{Ro}_F^{-1} = 40$ , the effect of rotation becomes more pronounced, and the flow is invariant in  $y$  at all values of  $\text{Ri}_F$ . (Figs. 4.2-4.4). We see that even the more strongly stratified simulations are affected by rotation. In addition, they all look much less turbulent than their more slowly rotating counterparts. This may be explained by the Taylor-Proudman theorem which states that the fluid motion is invariant along the axis of rotation at sufficiently large rotation rates. The Taylor-Proudman constraint suppresses the secondary instabilities that would normally take place in non-rotating systems.

Table 4.1: Simulations and selected quantities. The quantity  $\langle wT \rangle$  is discussed in detail in Section 4.5. Note that the ones marked by asterisk \* are initialized from the laminar steady state solution  $\mathbf{u}(z) = U_L \sin(z)\hat{\mathbf{e}}_x$ . For these ones at least, the initial conditions do not seem to affect simulations in a meaningful way.

$\text{Pe}_F$	$\text{Ro}_F^{-1}$	$\text{Ri}_F$	$u_{\text{rms}}$	$v_{\text{rms}}$	$\pm$	$w_{\text{rms}}$	$\pm$	$\langle wT \rangle$	$\pm$
0.1	0.2	1	1.804	$1.744 \times 10^{-1}$	$9.356 \times 10^{-1}$	$9.312 \times 10^{-2}$	$1.178$	$8.836 \times 10^{-2}$	$1.711 \times 10^{-1}$
0.1	0.2	10	2.764	$1.063 \times 10^{-1}$	$1.094$	$5.767 \times 10^{-2}$	$9.980 \times 10^{-1}$	$4.810 \times 10^{-2}$	$1.700 \times 10^{-2}$
0.1	0.2	100	4.913	$6.953 \times 10^{-2}$	$1.117$	$3.453 \times 10^{-2}$	$8.854 \times 10^{-1}$	$3.073 \times 10^{-2}$	$4.023 \times 10^{-3}$
0.1	1	1	1.905	$1.155 \times 10^{-1}$	$1.106$	$5.113 \times 10^{-2}$	$1.436$	$1.220 \times 10^{-1}$	$1.185 \times 10^{-1}$
0.1	1	10	2.334	$2.485 \times 10^{-1}$	$1.083$	$7.763 \times 10^{-2}$	$1.123$	$8.790 \times 10^{-2}$	$4.070 \times 10^{-2}$
0.1	1	100	4.883	$2.317 \times 10^{-1}$	$1.140$	$6.504 \times 10^{-2}$	$9.648 \times 10^{-1}$	$6.011 \times 10^{-2}$	$6.461 \times 10^{-3}$
0.1	1	1000	$1.361 \times 10^1$	$3.763 \times 10^{-2}$	$1.109$	$2.011 \times 10^{-2}$	$8.253 \times 10^{-1}$	$1.732 \times 10^{-2}$	$1.043 \times 10^{-3}$
0.1	5	1	2.059	$2.943 \times 10^{-1}$	$1.197 \times 10^{-1}$	$6.122 \times 10^{-2}$	$2.148$	$2.699 \times 10^{-1}$	$8.586 \times 10^{-1}$
0.1	5	10	4.080	$9.047 \times 10^{-1}$	$9.633 \times 10^{-1}$	$3.362 \times 10^{-1}$	$1.472$	$3.595 \times 10^{-1}$	$1.326 \times 10^{-1}$
0.1	5	100	7.578	$1.111 \times 10^{-1}$	$1.312$	$7.026 \times 10^{-2}$	$1.357$	$6.974 \times 10^{-2}$	$7.878 \times 10^{-2}$
0.1	40	1	2.025	$2.603 \times 10^{-1}$	$2.523 \times 10^{-3}$	$1.376 \times 10^{-3}$	$2.192$	$2.502 \times 10^{-1}$	$3.127 \times 10^{-3}$
0.1	40	10	3.980	1.297	$7.250 \times 10^{-6}$	$1.266 \times 10^{-5}$	$1.317$	$7.860 \times 10^{-1}$	$2.293 \times 10^{-1}$
0.1	40	100	$2.105 \times 10^1$	$5.442 \times 10^{-1}$	$3.935 \times 10^{-5}$	$1.084 \times 10^{-5}$	$1.710$	$9.358 \times 10^{-1}$	$1.060 \times 10^{-1}$
*0.1	40	1	2.103	$2.624 \times 10^{-1}$	$1.753 \times 10^{-1}$	$5.589 \times 10^{-2}$	$2.259$	$2.578 \times 10^{-1}$	$1.191 \times 10^{-1}$
*0.1	40	10	4.058	1.312	$1.022 \times 10^{-3}$	$2.730 \times 10^{-3}$	$1.309$	$7.651 \times 10^{-1}$	$2.343 \times 10^{-1}$
*0.1	40	100	$2.106 \times 10^1$	$4.705 \times 10^{-1}$	$5.692 \times 10^{-2}$	$2.173 \times 10^{-2}$	$1.765$	$7.720 \times 10^{-1}$	$1.044 \times 10^{-1}$
									$8.702 \times 10^{-2}$

Figure 4.1: Linear stability analysis results with laminar flow parameters  $\text{Re}, \text{Pe}$  and forcing-based parameters  $\text{Re}_F, \text{Pe}_F$ . Plotted is the growth rate map (log color bar). Upper: this is the linear stability using the laminar parameters  $\text{Re} = 10^4, \text{Pe} = 10^3$ . The green crosses denote the set of parameters with which numerical simulations in Section 4 were run. Lower: this is the linear stability using the turbulent parameters  $\text{Re}_F = 10^2, \text{Pe}_F = 0.1$ . The blue crosses denote the predicted locations of the same simulations in the parameter space once turbulence has fully developed. Some of the simulations outside the range are not plotted in the lower panel.

(a)



(b)

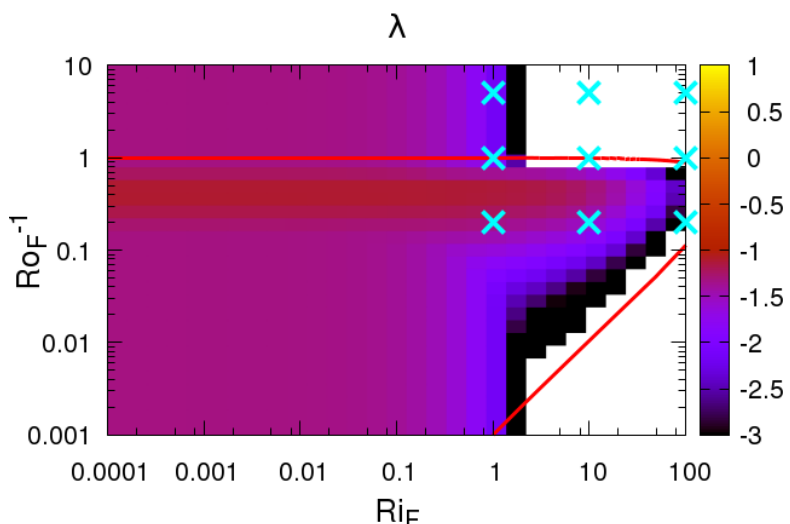


Figure 4.2: Characteristic snapshots of flow in the  $x$ -direction from simulation data for  $\text{Pe}_F = 0.1$  ( $\text{Pe} = 10$ ). From top to bottom:  $\text{Ro}_F^{-1} = 40, 5, 0.2$  ( $\text{Ro}^{-1} = 0.4, 0.05, 0.002$ ). From left to right:  $\text{Ri}_F = 1, 10, 10^2$  ( $\text{Ri} = 10^{-4}, 10^{-3}, 10^{-2}$ ). The snapshots of simulations with  $\text{Ro}_F^{-1} = 1$  ( $\text{Ro}^{-1} = 0.01$ ) are omitted as they looked very similar to those of  $\text{Ro}^{-1} = 0.2$  ( $\text{Ro}^{-1} = 0.002$ ) ones.

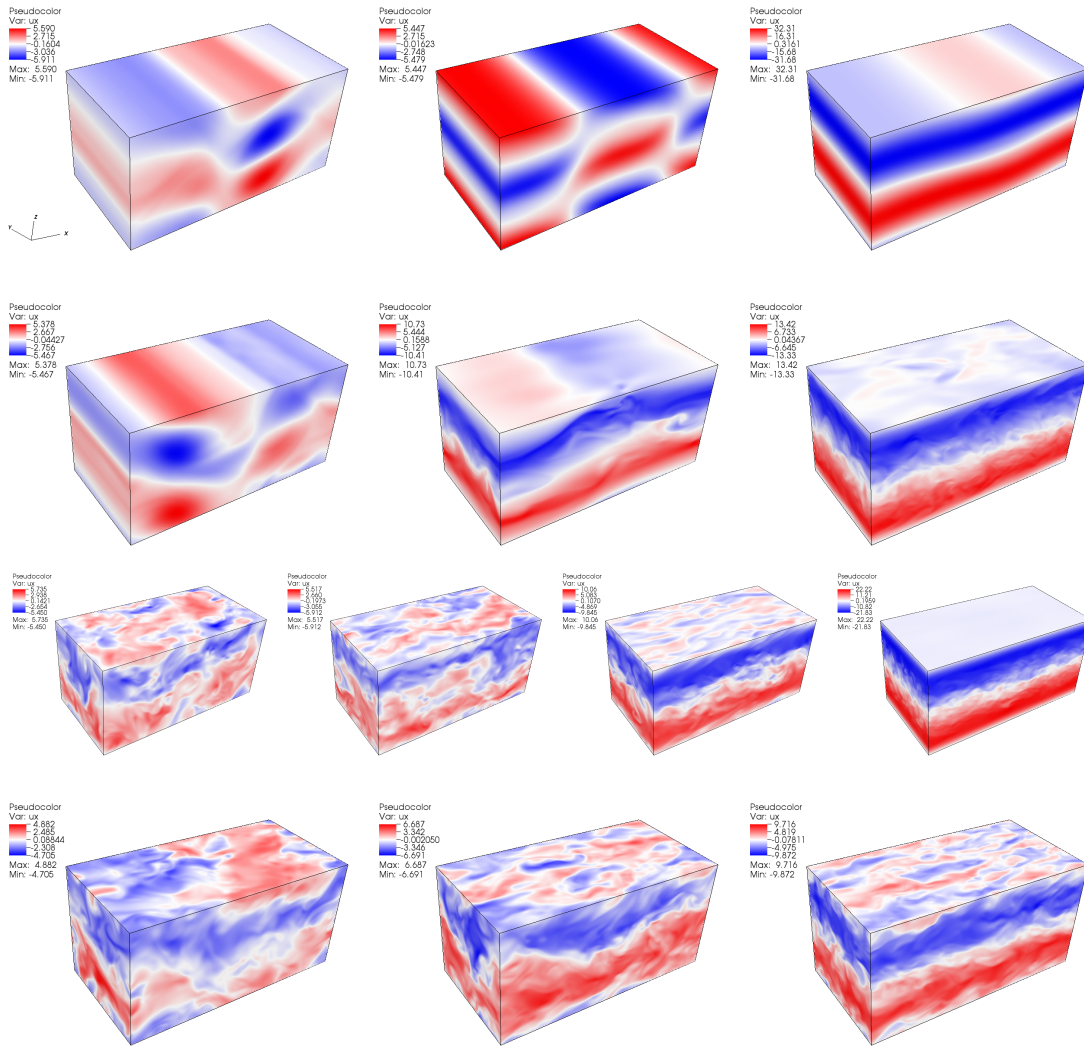


Figure 4.3: Characteristic snapshots of flow in the  $y$ -direction from simulation data for  $\text{Pe}_F = 0.1$  ( $\text{Pe} = 10$ ). From top to bottom:  $\text{Ro}_F^{-1} = 40, 5, 0.2$  ( $\text{Ro}^{-1} = 0.4, 0.05, 0.002$ ). From left to right:  $\text{Ri}_F = 1, 10, 10^2$  ( $\text{Ri} = 10^{-4}, 10^{-3}, 10^{-2}$ ). The snapshots of simulations with  $\text{Ro}_F^{-1} = 1$  ( $\text{Ro}^{-1} = 0.01$ ) are omitted as they looked very similar to those of  $\text{Ro}^{-1} = 0.2$  ( $\text{Ro}^{-1} = 0.002$ ) ones.

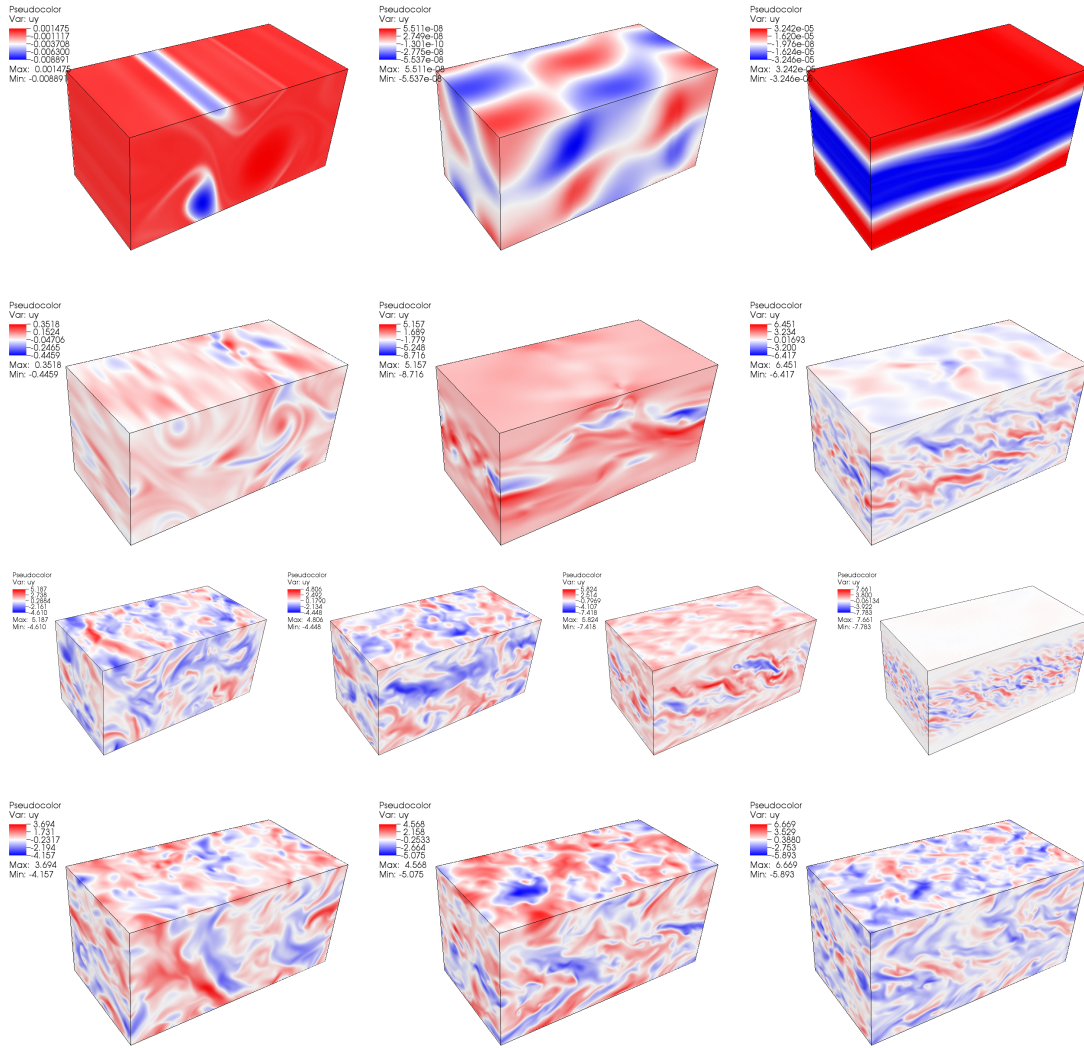
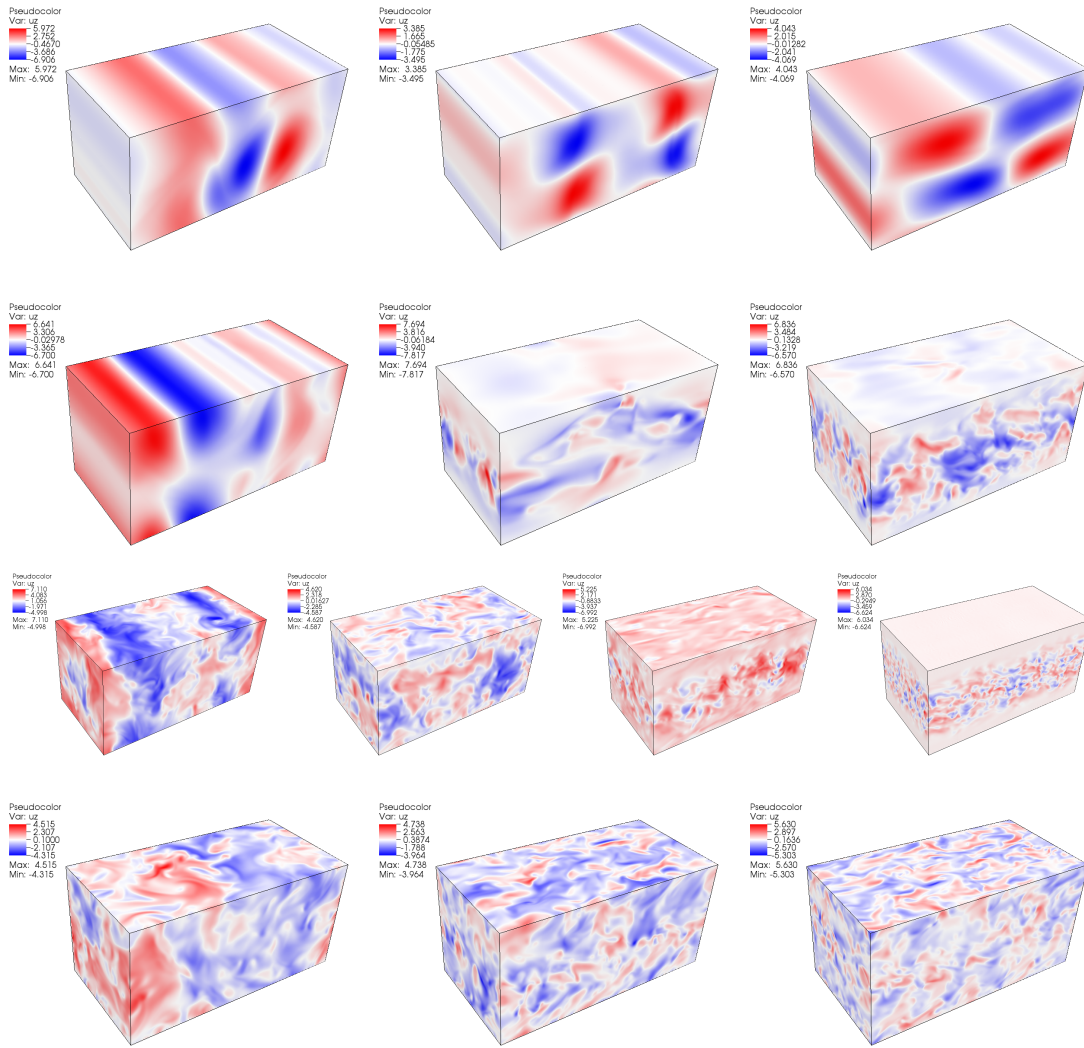


Figure 4.4: Characteristic snapshots of flow in the  $z$ -direction from simulation data for  $\text{Pe}_F = 0.1$  ( $\text{Pe} = 10$ ). From top to bottom:  $\text{Ro}_F^{-1} = 40, 5, 0.2$  ( $\text{Ro}^{-1} = 0.4, 0.05, 0.002$ ). From left to right:  $\text{Ri}_F = 1, 10, 10^2$  ( $\text{Ri} = 10^{-4}, 10^{-3}, 10^{-2}$ ). The snapshots of simulations with  $\text{Ro}_F^{-1} = 1$  ( $\text{Ro}^{-1} = 0.01$ ) are omitted as they looked very similar to those of  $\text{Ro}^{-1} = 0.2$  ( $\text{Ro}^{-1} = 0.002$ ) ones.



## 4.4 Quantitative analysis: mean flow

Having discussed the qualitative aspect of numerical results, we now turn to the quantitative analysis of data. In what follows, we define the mean flow as the flow velocity averaged over  $xy$ -plane:

$$\bar{u}(z, t) = \frac{1}{L_x L_y} \iint u(\mathbf{x}, t) dx dy \quad (4.4)$$

and the notation  $\bar{q}$  shall be used for the horizontal average of any other quantity  $q$  as well. We first examine the mean flow profiles in the weakly rotating limit of  $\text{Ro}_F^{-1} = 0.2$ . Fig. 4.5 shows instantaneous mean flow profiles at different times. When weakly stratified, the profile is noticeably variable but has a well-defined sinusoidal mean flow. At higher stratification, the mean flow has “pointy” maximum and minimum, although the profile seems to be almost steady. As stratification increases, the amplitude of the mean flow becomes larger since the turbulent viscosity decreases with the turbulent eddy scale as mentioned in the discussion of characteristic snapshots above, and studied in more detail later in this section. This is in agreement with previous results by Garaud and Kulenthirarajah (2016).

As we increase the rotation rate ( $\text{Ro}_F^{-1} = 1, 5$ ), the dichotomy between weakly and strongly stratified flows becomes more pronounced. For the weakly stratified case, we observe some variability, but the mean flow remains roughly sinusoidal in the instantaneous profiles. However, when strongly stratified, the flow profiles become increasingly asymmetric. This is consistent with the observations of the snapshots of the flow pre-

Figure 4.5: Mean flow profile in the  $x$ -direction from simulation data for  $\text{Pe}_F = 0.1$  ( $\text{Pe} = 10$ ). From top to bottom:  $\text{Ro}_F^{-1} = 40, 5, 0.2$  ( $\text{Ro}^{-1} = 0.4, 0.05, 0.002$ ). From left to right:  $\text{Ri}_F = 1, 10, 10^2, 10^3$  ( $\text{Ri} = 10^{-4}, 10^{-3}, 10^{-2}, 10^{-1}$ ). Each line corresponds to a different snapshot in time.

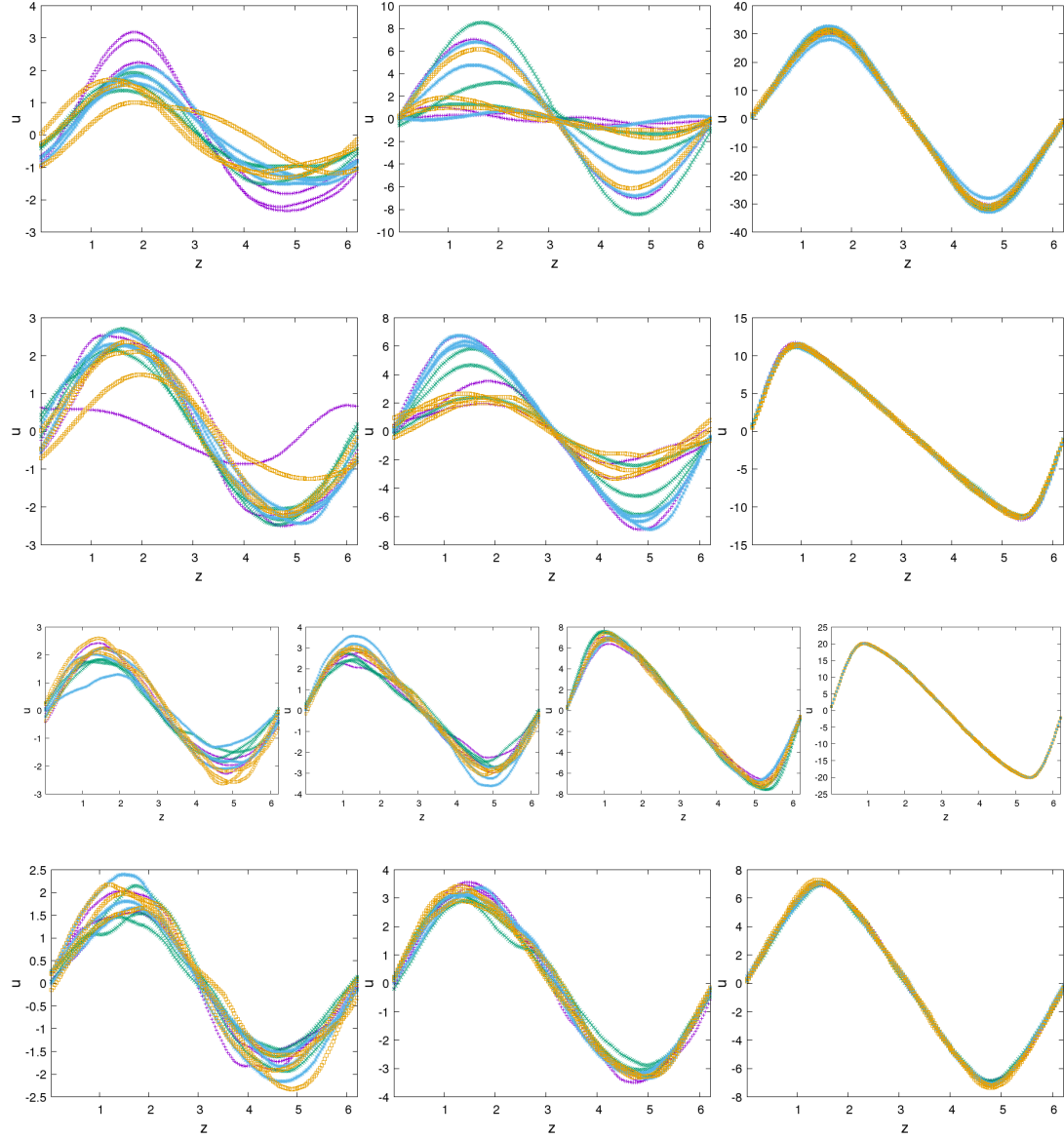
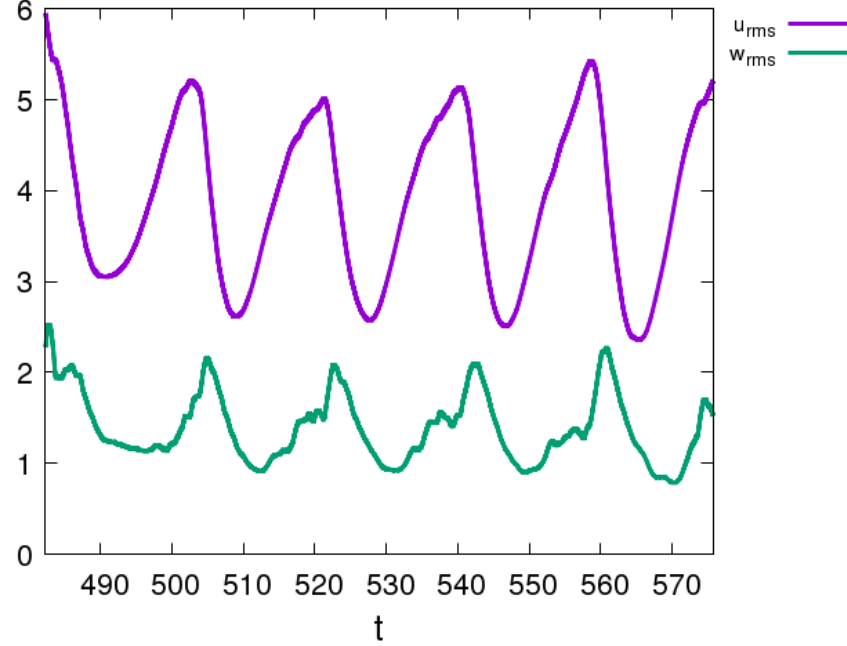


Figure 4.6: Time series of root-mean-square flow amplitudes for the simulation of  $Ri_F = 10$ ,  $Ro_F^{-1} = 5$ .



sented in Section 4, where we saw that turbulence is localized in the middle of the domain where the sign of shear is negative while the flow is close to laminar at the top and the bottom where the sign of shear is positive (Figs. 4.2-4.4). The mean shear is also weaker in the middle of the domain and stronger at the top and bottom of the domain.

To understand this, note that the horizontal average of the dimensional momentum equation is of the form:

$$\frac{\partial \bar{u}}{\partial t} + \frac{d}{dz}(\bar{u}\bar{w}) = \nu \frac{\partial^2 \bar{u}}{\partial z^2} + \frac{F_0}{\rho_m} \sin(k_s z), \quad (4.5)$$

where  $\overline{uw}$  is the Reynolds stress. In turbulence theory, it is commonly assumed that:

$$\overline{uw} = -\nu_{\text{turb}} \frac{d\bar{u}}{dz}, \quad (4.6)$$

in which case the horizontally averaged equation becomes:

$$\frac{\partial \bar{u}}{\partial t} = \frac{\partial}{\partial z} \left[ (\nu + \nu_{\text{turb}}) \frac{\partial \bar{u}}{\partial z} \right] + \frac{F_0}{\rho_m} \sin(k_s z). \quad (4.7)$$

In a statistically steady state, integration in  $z$  yields the following:

$$C' = (\nu + \nu_{\text{turb}}) \frac{d\bar{u}}{dz} - \frac{F_0}{\rho_m k_s} \cos(k_s z). \quad (4.8)$$

This shows that the amplitude of the mean flow depends on  $\nu_{\text{turb}}$ , and that the shear needs to be weaker in turbulent regions, while the shear will be stronger in laminar regions.

In addition, at the rotation rate of  $\text{Ro}_F^{-1} = 5$  and intermediate stratification of  $\text{Ri}_F = 10$ , we observe much larger variability in the mean flow suggestive of intermittency. To confirm this, we show in Fig. 4.6 the root-mean-square amplitude in  $u$  and  $w$  as functions of time. It is clear that the system undergoes intermittent dynamics that are reminiscent of a predator-prey oscillator, where the mean flow for which  $u_{\text{rms}}$  is a prey grows naturally due to the forcing while the turbulence for which  $w_{\text{rms}}$  is a predator has low amplitude. However, past a certain threshold, new instabilities can grow and feed on the energy from the mean flow thereby increasing  $w_{\text{rms}}$ , and reducing

$u_{\text{rms}}$ . Once  $u_{\text{rms}}$  drops below some threshold these instabilities are no longer excited and  $w_{\text{rms}}$  drops, allowing the mean flow to grow again.

Interestingly, this intermittency is not of the same kind as the one described by Kulenthirarajah and Garaud (2018), where the  $w_{\text{rms}}$  periodically drops to almost 0. Here instead it oscillates between a “low state” and a “high state”, which visually seem to correspond to a GSF-like mode and a shear-like modes, respectively.

To see this more quantitatively, we assume that the amplitude of the measured mean flow  $\bar{U}$  is approximately equal to  $\sqrt{2}u_{\text{rms}}$ . We can then calculate the effective parameters of the system as:

$$\text{Re}_{\text{eff}} = \frac{\bar{U}}{k_s \nu} = \frac{(\bar{U}/U_F)U_F}{k_s \nu} = \left( \sqrt{2}u_{\text{rms}} \right) \text{Re}_F, \quad (4.9)$$

and similarly,

$$\begin{aligned} \text{Ri}_{\text{eff}} &= \left( \frac{1}{2u_{\text{rms}}^2} \right) \text{Ri}_F, \\ \text{Pe}_{\text{eff}} &= \left( \sqrt{2}u_{\text{rms}} \right) \text{Pe}_F, \\ \text{Ro}_{\text{eff}} &= \left( \sqrt{2}u_{\text{rms}} \right) \text{Ro}_F. \end{aligned} \quad (4.10)$$

Note that  $\bar{U}$  is dimensional but  $u_{\text{rms}}$  is non-dimensional. These effective parameters therefore fluctuate as the amplitude of the mean flow varies with time. Plotted in Fig. 4.7 is the track made by each simulation as it moves around in parameter space, overlaid on a linear stability plot made at parameters  $\text{Re}_F = 100$  and  $\text{Pe}_F = 0.1$ <sup>1</sup>. The track we

---

<sup>1</sup>This ignores the fact that  $\text{Re}_{\text{eff}}$  and  $\text{Pe}_{\text{eff}}$  are not equal to 100 and 0.1, respectively, but the results

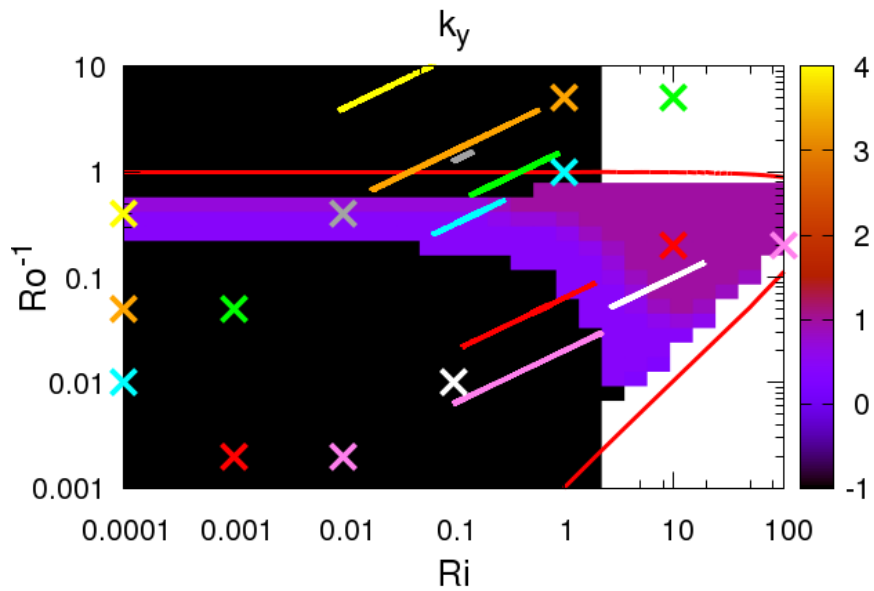
are interested in here is the green track in Fig. 4.7. The two green crosses on either side of this track correspond to assuming that the mean flow amplitude is either the laminar amplitude  $U_L$  or the turbulent flow amplitude  $U_F$ , respectively. As we can see from the maps, the track straddles two different dynamical regions, namely the GSF “wedge” and the shear instability region. Hence, this simulation exhibits a periodic transition from strong 2D shear flow instabilities to weaker GSF instability thus explaining the observed intermittency.

For the high rotation rate of  $\text{Ro}_F^{-1} = 40$ , we similarly see huge variability at weaker stratification values. Instead of being intermittent, these exhibit wave-like quasi-periodic behavior. At the strongly stratified limit, a well-defined “pointy” mean flow is observed similar to the very weakly rotating limit. This recovery of symmetry is expected as they are identified to be 2D from the characteristic snapshots, and as they lie in the region of parameter space linearly unstable to shearing modes.

---

are not too dependent on the Reynolds and Péclet numbers selected.

Figure 4.7: Time variation of effective system parameters for selected simulations overlaid on the linear stability maps for  $Re_F = 100$  and  $Pe_F = 0.1$ . Crosses in the bottom left corner denote the laminar parameters  $Ri, Ro^{-1}$  and the ones of the same color in the top right corner denote the forcing-based parameters  $Ri_F, Ro_F^{-1}$ . The line stretching in between the two crosses correspond to the effective system parameters  $Ri_{\text{eff}}, Ro_{\text{eff}}^{-1}$ .



## 4.5 Quantitative analysis: heat transport

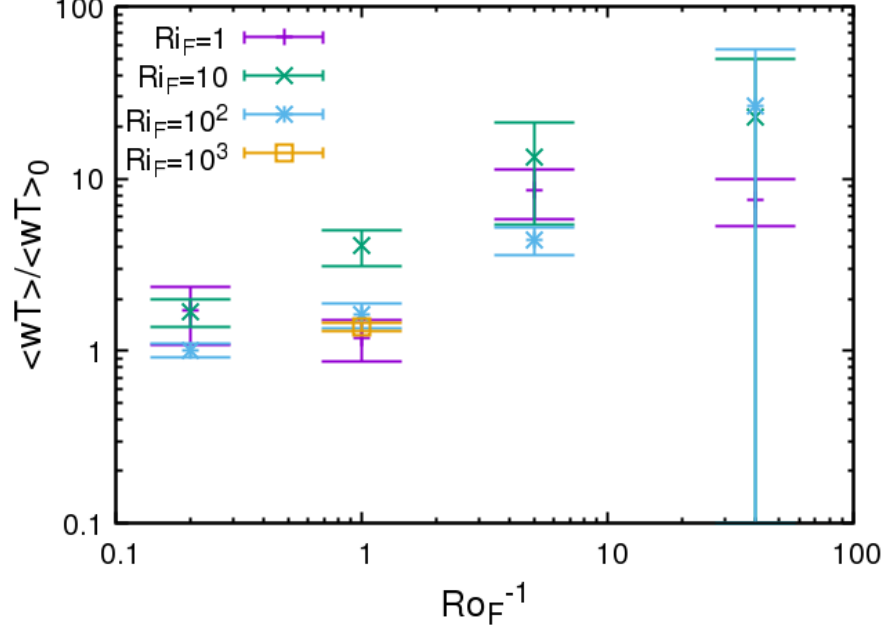
We now turn to a more quantitative analysis of the heat transport. First, we define the statistical mean over volume and over time for a quantity  $q$  as:

$$\langle q \rangle = \frac{1}{t_2 - t_1} \int_{t_1}^{t_2} \left[ \frac{1}{L_x L_y L_z} \iiint q(\mathbf{x}, t) d^3 \mathbf{x} \right] dt, \quad (4.11)$$

where  $t_1$  and  $t_2$  are two times from the statistically stationary state, and  $L_x, L_y$  and  $L_z$  denote the non-dimensional lengths of the computational domain in  $x, y$  and  $z$  respectively. Fig. 4.8 shows the mean heat flux  $\langle wT \rangle$  normalized against the mean heat flux of the non-rotating case  $\langle wT \rangle_0$  (whose values are taken from Garaud and Kullen-thirarajah 2016) as a function of the non-dimensional rotation rates  $\text{Ro}_F^{-1}$ . We see that  $\langle wT \rangle / \langle wT \rangle_0$  generally increases as rotation rate increases. This can be explained by the existence of coherent large-scale rolls seen in Figs. 4.2-4.4. Unlike small turbulent eddies that can be aligned in arbitrary directions, these rolls have a well-defined alignment that allows for more efficient mixing.

This result is interesting, and suggests that rotational instabilities could be a significant source of heat transport in stars, which is not usually taken into account in stellar evolution models.

Figure 4.8: Normalized mean heat flux  $\langle wT \rangle / \langle wT \rangle_0$  as a function of the rotation rate  $\text{Ro}_F^{-1}$ . Some error bars at  $\text{Ro}_F^{-1} = 40$  are greater than the quantity itself in magnitude so that they appear to extend to the bottom of the plot.



## 4.6 Quantitative analysis: turbulent momentum transport

We now turn to a quantitative analysis of momentum transport. Fig. 4.9 shows the plots of  $\overline{uw}$  vs.  $d\bar{u}/dz$  based on Eqn. 4.6. In the weakly rotating limit, the relationship between  $\overline{uw}$  and  $d\bar{u}/dz$  is close to linear, especially for weak stratification.

At a little higher rotation rate of  $\text{Ro}_F^{-1} = 1$ , however, we notice that  $\overline{uw}$  becomes a nonlinear function of the shear as we increase  $\text{Ri}_F$ . At the highest value of stratification,  $\overline{uw}$  is almost zero in the region where  $d\bar{u}/dz$  is positive, implying a reduced amount of turbulence by positive angular momentum gradient. Meanwhile, when  $d\bar{u}/dz < 0$ , the value of  $\overline{uw}$  linearly increases with the magnitude of the shear. This exactly corresponds to the localization of turbulence due to GSF instabilities we

saw from the characteristic snapshots in Fig. 4.2.

In the rapidly rotating limit ( $\text{Ro}_F^{-1} = 40$ ), the profiles have significant amount of variability and lack a definite shape. This is again explained by the fact that the dynamics are dominated by rotational waves, that transport momentum back and forth between the mean flow and the perturbations.

To understand this more quantitatively, we estimate the value of  $\nu_{\text{turb}}$  by fitting the  $\bar{uw}$  vs.  $d\bar{u}/dz$  data with a linear function of the kind  $f(x) = -ax$ , and letting  $\nu_{\text{turb}} = a$ . For the profiles which are close to linear, the fitting recovers the standard assumption for  $\nu_{\text{turb}}$  given in 4.6. For the profiles that are not linear,  $\bar{uw}$  is a function that strongly depends on the sign of the shear, and thus we measure turbulent viscosity  $\nu_-$  in the region of negative shear  $d\bar{u}/dz < 0$  and turbulent viscosity  $\nu_+$  in the region of positive shear  $d\bar{u}/dz > 0$  separately. We focus on the cases which are in the shear-unstable or GSF-unstable, where the  $\bar{uw}$  vs.  $d\bar{u}/dz$  profiles are relatively steady, but omit the cases which are strongly dominated by rotation where fitting a linear function is not meaningful.

Tab. 4.2 presents  $\nu_-$  and  $\nu_+$  values thus extracted and Fig. 4.10 shows this visually. At the low rotation rate of  $\text{Ro}_F^{-1} = 0.2$ , we recover results similar to those of Garaud and Kulenthirarajah (2016) within uncertainty. Interestingly, we find that the value of  $\nu_{\text{turb}}$  does not change significantly as we increase the rotation rate to  $\text{Ro}_F^{-1} = 1$  at low stratification. This might seem surprising, given that at  $\text{Ro}_F^{-1} \sim 1$  we would have expected to see non-negligible effects of rotation and it indeed lies in the region of GSF instabilities in Fig. 4.7. This may be explained by the fact that the growth rates of

GSF instabilities are only slightly larger than those of shear instabilities, as we can see from Fig. 4.1, which might allow for the effect of shearing modes to be significant even in the GSF “wedge”.

For higher values of stratification, however, rotation seems to take considerable effect on the value of turbulent viscosity. It is not entirely clear whether  $\nu_-$  increases or decreases as the rotation rate increases. On the other hand,  $\nu_+$  clearly decreases as the rotation rate increases. This trend, again, is characteristic of GSF instabilities where positive shear stabilizes the system and turbulence disappears. Therefore, at higher stratification values, turbulent viscosity seem to be increasingly affected by the rotation rate. This is reasonable given the GSF “wedge” in Fig. 4.1 extends to the lower values of  $\text{Ro}_F^{-1}$  at higher values of  $\text{Ri}_F$ .

In conclusion, Zahn’s model of turbulent diffusion is found to be valid when the effect of rotation is negligible. However, we find that simulations of higher values of  $\text{Ro}_F^{-1}$  are substantially affected by the rotation. Hence Zahn’s mixing model does not seem to apply and instead one must apply turbulent mixing prescriptions appropriate for GSF instabilities that depend on the sign of the shear at intermediate value of rotation rate, as well as the quasi-periodic waves in rapidly rotating limit.

Figure 4.9:  $\bar{uw}$  vs.  $d\bar{u}/dz$  from simulation data for  $\text{Pe}_F = 0.1$  ( $\text{Pe} = 10$ ). From top to bottom:  $\text{Ro}_F^{-1} = 40, 5, 0.2$  ( $\text{Ro}^{-1} = 0.4, 0.05, 0.002$ ). From left to right:  $\text{Ri}_F = 1, 10, 10^2, 10^3$  ( $\text{Ri} = 10^{-4}, 10^{-3}, 10^{-2}, 10^{-1}$ ). Each line corresponds to a different time.

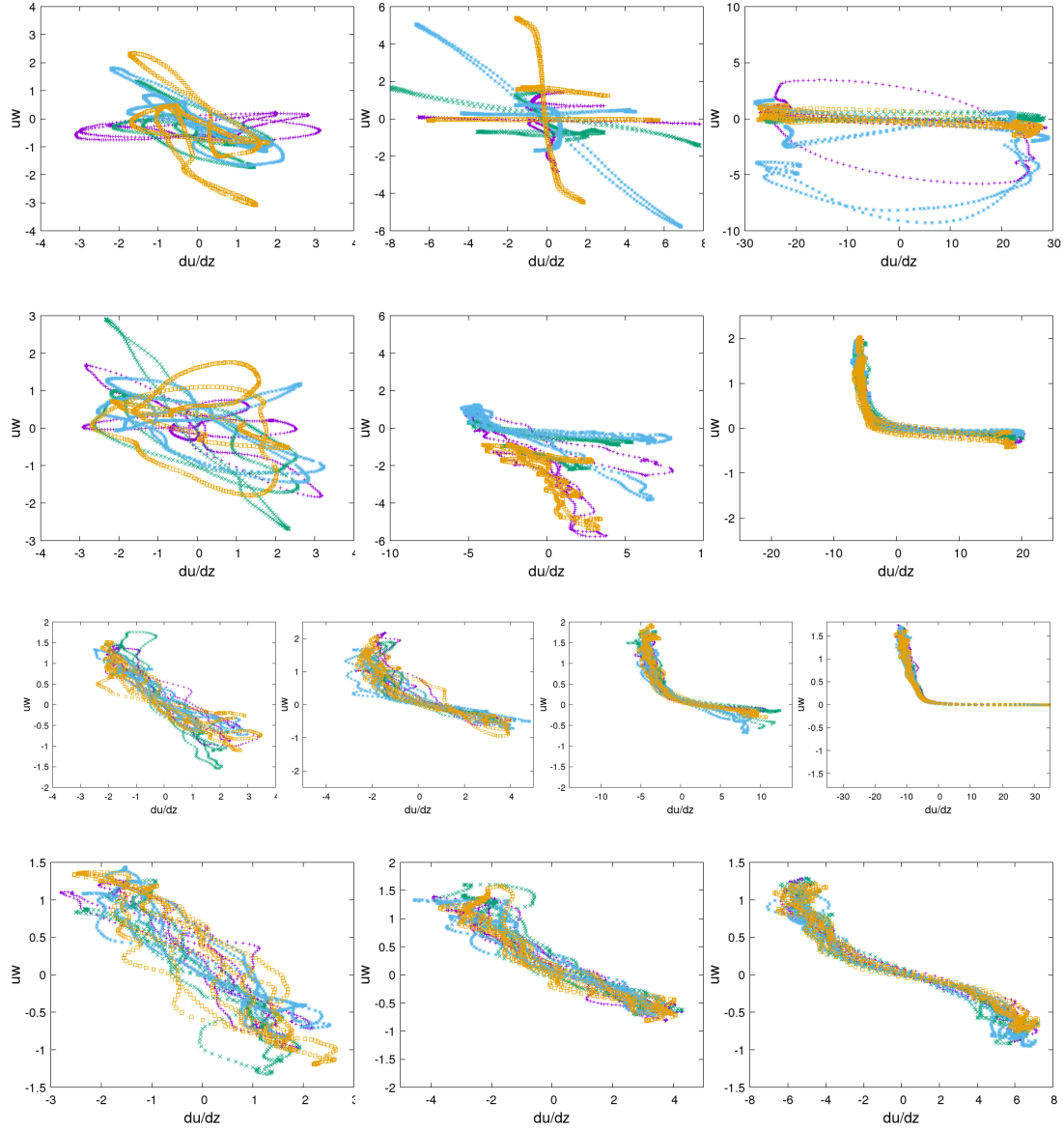
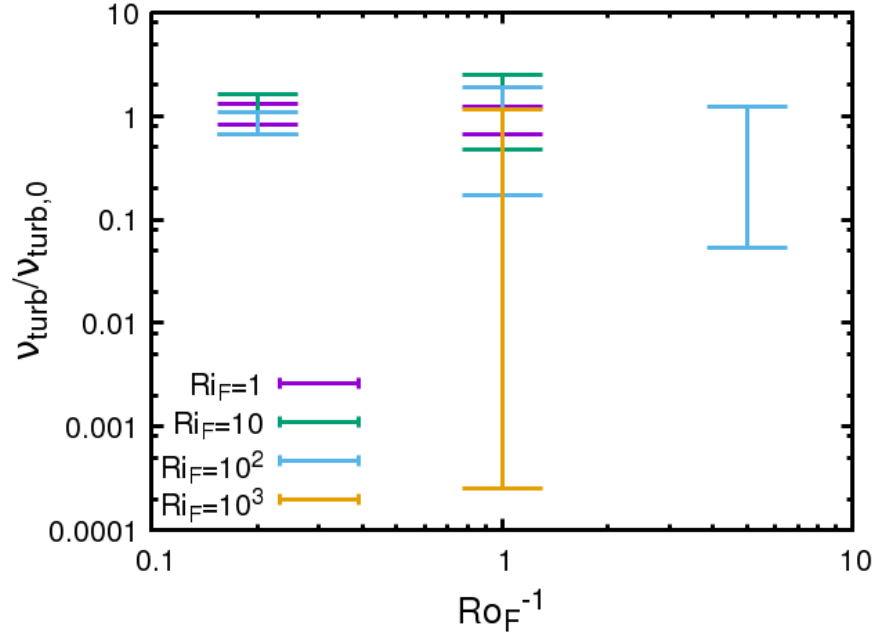


Table 4.2: Values of  $\nu_{\text{turb}}$  extracted from the simulations. Non-rotating ones are taken from Garaud et al. (2017). Note that  $\nu_- = \nu_+$  since the profile is symmetric in the absence of rotation. Also note that generally  $\nu_- > \nu_+$  when rotation is present.

$\text{Ro}_F^{-1}$	$\text{Ri}_F$	$\nu_-$	$\nu_+$
0	1	$0.540 \pm 0.098$	
0	10	$0.264 \pm 0.038$	
0	$10^2$	$0.157 \pm 0.012$	
0	$10^3$	$0.064 \pm 0.005$	
0.2	1	$0.703 \pm 0.115$	$0.453 \pm 0.110$
0.2	10	$0.436 \pm 0.077$	$0.176 \pm 0.070$
0.2	$10^2$	$0.169 \pm 0.158$	$0.104 \pm 0.095$
1	1	$0.664 \pm 0.109$	$0.360 \pm 0.031$
1	10	$0.657 \pm 0.158$	$0.127 \pm 0.076$
1	$10^2$	$0.300 \pm 0.171$	$0.027 \pm 0.050$
1	$10^3$	$0.073 \pm 0.150$	$0.000 \pm 0.008$
5	$10^2$	$0.196 \pm 0.346$	$0.009 \pm 0.013$

Figure 4.10: Normalized turbulent viscosity  $\nu_{\text{turb}}/\nu_{\text{turb},0}$  as a function of the rotation rate  $\text{Ro}_F^{-1}$ . The highest point of the error bar denotes  $\nu_-/\nu_{\text{turb},0}$ ; the lowest point of the error bar denotes  $\nu_+/\nu_{\text{turb},0}$ .



# Section 5

## Conclusion

In this work, we studied the stability of rotating, stably stratified shear flows at low Péclet number. In doing so, we used two methods: linear stability analysis and direct numerical simulations. In the very weakly rotating limit, we recovered the results of previous studies (Townsend, 1958; Balmforth and Young, 2002; Garaud et al., 2015; Garaud and Kulenthirarajah, 2016; Garaud et al., 2017; Gagnier and Garaud, 2018).

As rotation increases, linear stability reveals the existence of a dynamically different region of parameter space where linearly-unstable modes are invariant along the azimuthal direction. These are GSF modes. Numerical simulations show that turbulence is localized in regions of negative shear at higher  $\text{Ri}_F$ , consistent with the known dynamics of GSF instabilities.

In the rapidly rotating limit, we observe another transition of dynamics. Linear stability result shows the dynamics shifts from GSF instabilities back to the 2D regime of diffusive stratified shear instabilities. In this regime, we found the numerical simulations

to be dominated by the effect of rotation to an extent where Taylor-Proudman theorem applies.

A quantitative analysis of the simulation data showed nearly identical results in the very weakly rotating limit to those of non-rotating simulations by Garaud and Kulenthirarajah (2016). As we increase the rotation rate, we found the mean flow profile to become asymmetric, corresponding to the localization of turbulence. We also found an interesting intermittent behavior that switches between diffusive stratified shear instabilities and GSF instabilities at the intermediate value of both rotation rate and stratification ( $\text{Ro}_F^{-1} = 5$ ,  $\text{Ri}_F = 10$ ). In the rapidly rotating limit, we observed huge variability in the mean flow at lower  $\text{Ri}_F$ , and a recovery of symmetric profile at higher  $\text{Ri}_F$ , consistent with the linear analysis results.

Regarding the heat transport, we discovered that rotational instabilities may be a substantial source of heat transport in stars with large rotation rates.

Regarding the momentum transport, our results in the weakly rotating limit are in agreement with those of previous study (see 4.2) that Zahn's mixing model is appropriate (Garaud and Kulenthirarajah, 2016). In Fig. 4.9, however, we saw that the sign of the shear is crucial in setting the amount of turbulence when the system is in the region of parameter space significantly affected by GSF instabilities. Zahn's model of turbulent diffusivity does not take account of the sign of the shear. Therefore, his model cannot be applied when the dominant dynamics consist of rotational waves and instabilities, especially GSF-like ones. This result is not entirely surprising, but demonstrates that a key aspect of the problem lies in identifying the boundary between the

shear-dominated and GSF-dominated dynamics. In this respect, we have demonstrated that linear theory is sometimes (but not always) able to predict the position of that boundary, even when it is applied to a mean flow that is laminar.

For instance, we revisit the discussion of the intermittent simulation at intermediate rotation rate and intermediate stratification in Section 4.4. Various aspects of the numerical simulation (e.g. mean flow, time series of root-mean-square velocities, amount of turbulence as a function of shear) point to intermittency. In the linear stability map of Fig. 4.7, the effective parameters of this simulation indeed range between two regions that are dynamically distinct, which explains the origin of the observed intermittency. This is not the only simulation that shows correspondence between the results of a linear analysis performed on the actual mean flow, and the numerical simulations. In fact, this statement seems to apply to a number of our simulations. This is somewhat unexpected, since linear stability analysis is only strictly valid when the background flow is laminar. However, our findings suggest that this is true even for turbulent background flows, although approximately. Therefore, for some simulations, it is possible to establish whether a flow profile is shear-unstable or GSF-unstable simply by performing such an analysis, even if that flow is already turbulent.

On the other hand, there are simulations that do not show exact correspondence to their linear stability counterparts. For example, we look at the simulation of  $Ri_F = 1$  and  $Ro_F^{-1} = 1$ , whose effective parameters clearly lie in the GSF “wedge” (blue in Fig. 4.7). We would expect this simulation to be dominated by GSF instabilities according to linear stability analysis, but the quantitative analysis shows fairly sym-

metric profile of  $\overline{uw}$  vs.  $d\bar{u}/dz$ . This might be due to the fact that the growth rates of GSF modes are commensurate in magnitude to those of shearing modes (Fig. 3.1). However, it is not entirely clear if this argument is sufficient to explain the absence of GSF characteristics in this simulation. Therefore, we conclude that more work is needed to further investigate this issue—whether linear stability analysis of turbulent flows is viable.

In this model, we have neglected the effects of compositional stratification and magnetic forces. In addition, we assumed ideal conditions where the background temperature gradient is uniform, the forcing is sinusoidal and unidirectional, and the Cartesian domain lies in the equator and is periodic in all directions. The goal of future studies would be to understand the effect of these assumptions on the rotational instabilities and corresponding mixing.

Finally, in this study we have only focused on regions that are linearly unstable either to the diffusive stratified shear instabilities or the GSF instabilities. It would be interesting to explore the non-linear dynamics and mixing caused by subcritical instabilities in regions regarded as linearly stable.

# Bibliography

- Anagnos, J. J. and Desoer, C. A. (1991). An elementary proof of the Routh-Hurwitz stability criterion. *Circuits, Systems and Signal Processing*, 10(1):101–114.
- Balmforth, N. J. and Young, Y.-N. (2002). Stratified Kolmogorov flow. *Journal of Fluid Mechanics*, 450:131–167.
- Barker, A. J., Jones, C. A., and Tobias, S. M. (2019). Angular momentum transport by the GSF instability: nonlinear simulations at the equator. *Monthly Notices of the Royal Astronomical Society*, 487(2):1777–1794. arXiv: 1905.06962.
- Deheuvels, S., García, R. A., Chaplin, W. J., Basu, S., Antia, H. M., Appourchaux, T., Benomar, O., Davies, G. R., Elsworth, Y., Gizon, L., Goupil, M. J., Reese, D. R., Regulo, C., Schou, J., Stahn, T., Casagrande, L., Christensen-Dalsgaard, J., Fischer, D., Hekker, S., Kjeldsen, H., Mathur, S., Mosser, B., Pinsonneault, M., Valenti, J., Christiansen, J. L., Kinemuchi, K., and Mullally, F. (2012). Seismic Evidence for a Rapidly Rotating Core in a Lower-giant-branch Star Observed with Kepler. *The Astrophysical Journal*, 756:19.
- Fricke, K. (1968). Instabilität stationärer Rotation in Sternen. *Zeitschrift für Astrophysik*, 68:317.
- Gagnier, D. and Garaud, P. (2018). Turbulent transport by diffusive stratified shear flows: from local to global models. Part II: Limitations of local models. *The Astrophysical Journal*, 862(1):36. arXiv: 1803.10455.
- Garaud, P., Gagnier, D., and Verhoeven, J. (2017). Turbulent Transport by Diffusive Stratified Shear Flows: From Local to Global Models. I. Numerical Simulations of a Stratified Plane Couette Flow. *The Astrophysical Journal*, 837:133.
- Garaud, P., Gallet, B., and Bischoff, T. (2015). The stability of stratified spatially periodic shear flows at low Péclet number. *Physics of Fluids*, 27:084104.
- Garaud, P. and Kulenthirarajah, L. (2016). Turbulent Transport in a Strongly Stratified Forced Shear Layer with Thermal Diffusion. *The Astrophysical Journal*, 821:49.
- Goldreich, P. and Schubert, G. (1967). Differential Rotation in Stars. *The Astrophysical Journal*, 150:571.

- Greenstein, J. L. and Richardson, R. S. (1951). Lithium and the Internal Circulation of the Sun. *The Astrophysical Journal*, 113:536.
- Howard, L. N. (1961). Note on a paper of John W. Miles. *Journal of Fluid Mechanics*, 10(4):509–512.
- Høiland, E. (1941). Avhandliger norske videnskaps-akademi i oslo, i. math naturv. *Klasse*, 11:1–24.
- Høiland, E. and Bjerknes, V. (1939). *On the interpretation and application of the circulation theorems of V. Bjerknes*. M. Johansen. Google-Books-ID: eKsSAQAAMAAJ.
- Kulenthirarajah, L. and Garaud, P. (2018). Turbulent Transport by Diffusive Stratified Shear Flows: From Local to Global Models. III. A Closure Model. *The Astrophysical Journal*, 864:107.
- Lignières, F., Califano, F., and Mangeney, A. (1999). Shear layer instability in a highly diffusive stably stratified atmosphere. *Astronomy and Astrophysics*, 349:1027–1036.
- Miles, J. W. (1961). On the stability of heterogeneous shear flows. *Journal of Fluid Mechanics*, 10(4):496–508.
- Moll, R. and Garaud, P. (2017). The Effect of Rotation on Oscillatory Double-diffusive Convection (Semiconvection). *The Astrophysical Journal*, 834:44.
- Olive, K. A., Steigman, G., and Walker, T. P. (2000). Primordial Nucleosynthesis: Theory and Observations. *Physics Reports*, 333-334:389–407. arXiv: astro-ph/9905320.
- Prat, V. and Lignières, F. (2013). Turbulent transport in radiative zones of stars. *Astronomy & Astrophysics*, 551:L3. arXiv: 1301.4151.
- Richardson, L. F. (1920). The Supply of Energy from and to Atmospheric Eddies. *Proceedings of the Royal Society of London Series A*, 97:354–373.
- Sengupta, S. and Garaud, P. (2018). The Effect of Rotation on Fingering Convection in Stellar Interiors. *The Astrophysical Journal*, 862:136.
- Sestito, P. and Randich, S. (2005). Time scales of Li evolution: a homogeneous analysis of open clusters from ZAMS to late-MS. *Astronomy and Astrophysics*, 442:615–627.
- Skumanich, A. (1972). Time Scales for CA II Emission Decay, Rotational Braking, and Lithium Depletion. *The Astrophysical Journal*, 171:565.
- Solberg, M. (1936). Le mouvement d'inertie de l'atmosphère stable et son rôle dans la théorie des cyclones. *Union Géodésique et Géophysique internationale VIeme assemblée, Edinburg*, pages 66–82.
- Spiegel, E. A. and Veronis, G. (1960). On the Boussinesq Approximation for a Compressible Fluid. *The Astrophysical Journal*, 131:442.

- Stellmach, S., Traxler, A., Garaud, P., Brummell, N., and Radko, T. (2011). Dynamics of fingering convection. Part 2 The formation of thermohaline staircases. *Journal of Fluid Mechanics*, 677:554–571.
- Townsend, A. A. (1958). The effects of radiative transfer on turbulent flow of a stratified fluid. *Journal of Fluid Mechanics*, 4(4):361–375.
- Traxler, A., Garaud, P., and Stellmach, S. (2011). Numerically Determined Transport Laws for Fingering (“Thermohaline”) Convection in Astrophysics. *The Astrophysical Journal*, 728(2):L29.
- Zahn, J.-P. (1974). Rotational instabilities and stellar evolution. volume 59, pages 185–194.
- Zahn, J.-P. (1992). Circulation and turbulence in rotating stars. *Astronomy and Astrophysics*, 265:115–132.